Modeling Transient Slag-Layer Phenomena in the Shell/mold Gap in Continuous Casting of Steel

YA MENG and BRIAN G. THOMAS

Mold-slag friction and fracture may cause heat-transfer variations in continuous casting, which leads to steel shell temperature and stress variations, resulting in surface cracks. Analytical transient models of liquid slag flow and solid slag stress have been coupled with a finite-difference model of heat transfer in the mold, gap, and steel shell to predict transient shear stress, friction, slip, and fracture of the slag layers. The models are validated by comparing with numerical models and plant measurements of mold friction. Using reported slag-fracture strength and time-temperature-transformation (TTT) diagrams, the models are applied to study the effect of casting speed and mold-powder viscosity properties on slag-layer behavior between the oscillating mold wall and the solidifying steel shell. The study finds that liquid-slag lubrication would produce negligible stresses. A lower mold-slag consumption rate leads to high solid friction and results in solid-slag-layer fracture and movement below a critical value. Crystalline slag tends to fracture near the meniscus and glassy slag tends to fracture near the mold exit. A medium casting speed may be the safest to avoid slag fracture, due to its having the lowest critical lubrication consumption rate. The high measured friction force in operating casters could be due to three sources: an intermittent moving solid slag layer, excessive mold taper, or mold misalignment.

I. INTRODUCTION

MANY phenomena in continuous casting, including the formation of surface defects, are greatly affected by heat transfer in the mold.[1–5] The interfacial slag layer(s) between the solidifying steel shell and the mold wall dominates the resistance to heat removal and, thus, controls mold heat transfer in powder casting.[6,7,8] Surface defects, such as longitudinal cracks and star cracks, have been attributed to variations of slag lubrication.[9,10] High meniscus heat transfer and variations in meniscus heat transfer correlate with increased surface or subsurface defects,[9,11,12] but the reasons are not understood. Thus, an improved understanding of slag-layer behavior is important for steel quality.

In continuous casting, mold powder is added to the free surface of the liquid steel. It sinters and melts, spreading over the liquid steel surface according to the steel-surface contour and flow pattern.[13] During each oscillation stroke, liquid slag is pumped from the meniscus into the gap between the steel shell and the mold wall, where it acts as a lubricant,[14,15] so long as it remains liquid. A solid slag layer forms against the mold wall. Its thickness increases greatly just above the meniscus, where it is called the slag rim. Depending on the composition and cooling rate of the mold slag, the microstructure of the multiple layers that form may be glassy, crystalline, or mixtures of both.[16,17] Figure 1 shows a typical schematic of this region of the continuous casting process.

A substantial fraction of the slag consumed in the mold is entrapped in oscillation marks moving down at the casting speed. When a solid layer stably attaches to the mold wall, the remaining slag consumed is from the flowing liquid layer and is here called "lubrication consumption."

Compared with oil lubrication, powder(/slag) lubrication leads to more uniform and usually lower heat transfer.[5,18] The heat flux across the interfacial gap depends on the slag-layer thermal properties[19,20,21] and thickness,[8,22] which is affected by slag properties such as melting, crystallization behavior, and temperature-dependent viscosity.[23,24] It is reported that slag conductivity dominates heat transfer across the crystalline layer, although radiation is very important across glassy and liquid layers.[21] High-solidification-temperature crystalline slag usually reduces mold heat transfer.[24] This is likely due to the lower conductivity of crystalline slag[25] and the thicker solid slag layer that accompanies the higher solidification temperatures.

The hydrostatic or "ferrostatic" pressure of the molten steel pushes the unsupported steel shell against the mold walls, causing friction between the steel shell and the oscillating mold wall. At the corners, the shell may shrink away to form a gap, so friction there is often negligible. However, friction at the bottom of the narrow faces becomes a significant source of friction if excessive taper squeezes the wide-face shell. Finally, misalignment of the mold and strand can cause friction, especially if the stroke is large. It has been proposed that friction may impede increased casting speed.[26] This work also investigates friction as a cause of fracturing of the solidified slag layer that produces a local heat-flux variation. The accompanying temperature and stress variations in the steel shell could lead to quality problems, such as shear tearing, sticking, and even breakouts.[27,28,29]. Ozgu and Kocatulum[30] and Geist[31] both report a "sawtooth" shaped temperature fluctuation low in the mold, which suggests solid-slag-layer fracture and sheeting from the mold wall.[32] Currently, mold friction measurements are evaluated mainly as a means to detect problems with the oscillation system, such as mold misalignment. If the friction signal can be better understood, friction monitoring could be used

YA MENG, Graduate Student, Department of Materials Science and Engineering, and BRIAN G. THOMAS, Professor, Department of Mechanical and Industrial Engineering, are with the University of Illinois at Urbana–Champaign, Urbana, IL 61801. Contact e-mail: bgthomas@uiuc.edu
Manuscript submitted February 10, 2003.

to identify the status of mold lubrication to predict surface defects[33] and to help prevent breakouts.[34]

Figure 2(a) shows a 20-cm-long piece of slag film taken from the corner of an operating caster mold. Many researchers believe that a glassy slag layer forms against the mold wall due to high cooling rates during initial contact of the molten slag with the water-cooled copper mold. A liquid layer is 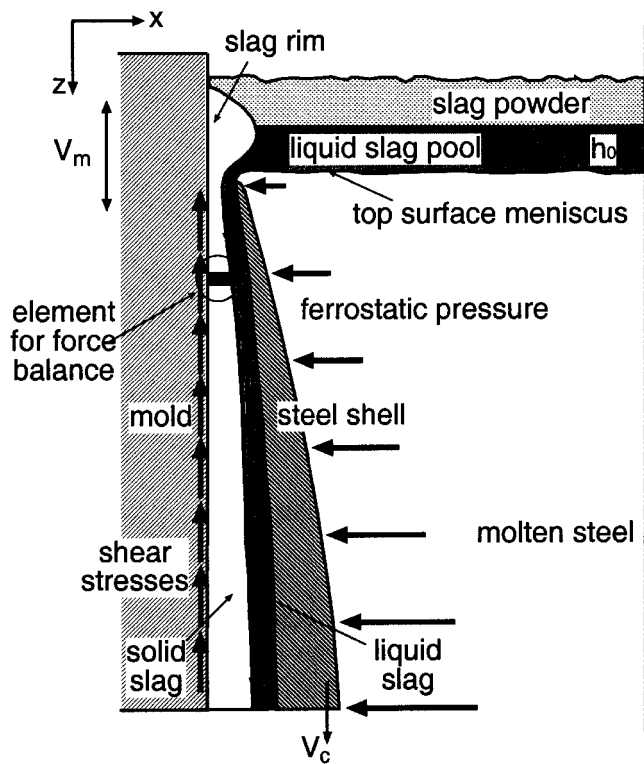present when the shell surface temperature is higher than the slag solidification temperature. Between these two layers, a crystalline layer is expected, according to the time-temperature-transformation (TTT) diagram, which has been measured recently in controlled laboratory conditions.[35,36] However, slag film samples taken from the mold wall usually show a different microstructure: a crystalline layer toward the mold side and glassy layer on the shell side,[25,32] as shown in Figure 2(b). Perhaps the glassy layer devitrifies during the long period when the solid layer attaches to the mold wall,[32] and perhaps the steel-side glassy layer forms from air quenching the liquid slag while obtaining the sample.

To understand and quantify these phenomena, it is necessary to simulate transport and stress in the molten and resolidified slag layers in the shell-mold gap. Models of steel solidification and heat transfer in continuous casting were reviewed previously.[37] Only a few models have detailed treatment of the interfacial layers. Of these, most assume a linear velocity distribution through the liquid-film thickness.[21,26,38,39] Several previous models have attempted to quantify gap flow by solving a Navier–Stokes equation.[28,40–49] In these models, the slag-layer thickness either is an input constant,[40,42,45,47,48] an input function,[43,49] or is assumed to be equal the shrinkage of the steel shell.[28,41,44,46] This ignores important phenomena such as ferrostatic pressure. Most previous models assume constant slag viscosity in the gap,[40,42,43,45,49,50] which is contrary to the tremendous temperature dependency reported in measurements[51–54] and the high-temperature gradient across the gap. Some researchers fit slag viscosity to a simple inverse function of temperature[28] or an Arrhenius equation.[41,44,47,51] However, the slag viscosity is only measured above the slag liquidus and is much lower on the mold side. Seldom have models discussed the effect of oscillation marks on lubrication and consumption. Moreover, no previous model describes the solid-layer fracture and sliding behavior of the slag layers. Thus, a more comprehensive model of interfacial gap lubrication and heat transfer was developed in this work.

Fig. 1—Schematic of interfacial gap phenomena in continuous casting mold.
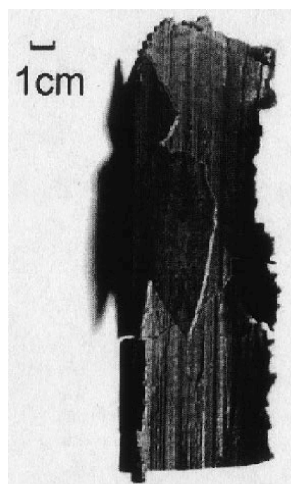
(a) macroscopic film including corner
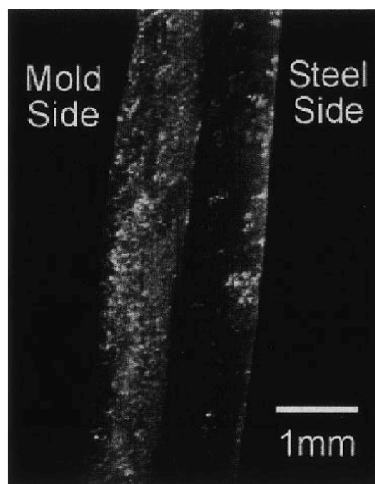
(b) crystalline and glassy layers
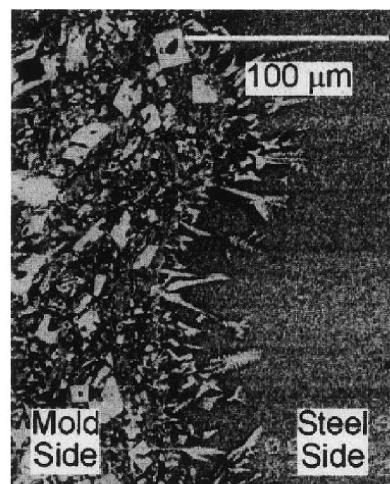
(c) close-up of the crystalline layer growing into glassy layer

Fig. 2—(a) through (c) Sample of slag layer and microstructure.

II. INTERFACE MODEL DESCRIPTION AND VALIDATION

The present work models heat transfer, liquid flow, and friction in the interfacial slag layers during an oscillation cycle. An analytical solution of the two-dimensional (2-D) momentum equation is derived for a temperature-dependent viscosity in the liquid slag layer. The model is validated through comparison with a numerical solution, based on the heat transfer calculated for typical casting conditions. Shear stress in the liquid slag layer is based on the velocity gradient and liquid viscosity. Next, the axial stress and friction in the solid slag layer are obtained by solving a force-balance equation. This model is validated using ANSYS.[56] Finally, CON1D, a FORTRAN program with combined heat-transfer, liquid-flow, and solid-friction models, is applied to predict typical behavior and critical conditions for fracture and sliding of the interfacial slag layers.

A. Heat-Transfer Model

The CON1D program, a simple but comprehensive model of heat transfer and solidification in continuous-cast steel, is used for the current study. The model includes a one-dimensional transient finite-difference calculation of heat conduction in the solidifying steel shell coupled with 2-D steady-state heat conduction in the mold wall. It features a detailed treatment of the interfacial gap between the shell and the mold, including mass and momentum balances on the slag layers and the effect of oscillation marks. Details of this model are presented elsewhere.[37]

B. Liquid Slag Layer Flow Model

For simplicity, the slag is treated as two layers, each with variable thickness in the vertical (z) direction: a rigid solid layer and a laminar liquid layer with temperature-dependent viscosity. A schematic profile of the mold, slag, and steel shell velocities is shown in Figure 3 for the case when the solid slag layer is stuck to the mold wall, so its
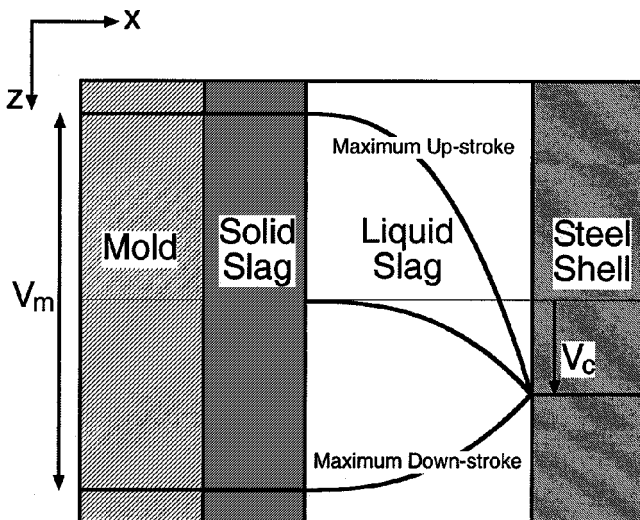
Fig. 3—Schematic profile of slag velocity during oscillation cycle.

average downward velocity (V_s) is zero. The steel shell moves downward at the casting speed V_c, and the mold oscillates in the vertical direction with the sinusoidal displacement function:

$$Z_m = Z_0 + \frac{s}{2}\sin(2\pi ft) \qquad [1]$$

A mass balance on the liquid slag layer gives the following continuity equation, assuming incompressible flow, constant density, and identical behavior within any vertical slice, so the velocity across the slab width (V_y) is zero:

$$\frac{\partial V_x}{\partial x} + \frac{\partial V_z}{\partial z} = 0 \qquad [2]$$

The following Navier–Stokes equation characterizes the laminar viscous flow of liquid slag vertically within the gap:

$$\rho_{slag} \cdot \left(\frac{\partial V_z}{\partial t} + V_x \cdot \frac{\partial V_z}{\partial x} + V_y \cdot \frac{\partial V_z}{\partial y} + V_z \cdot \frac{\partial V_z}{\partial z}\right)$$

$$= -\frac{\partial P}{\partial z} + \frac{\partial \tau_{xz}}{\partial x} + \frac{\partial \tau_{yz}}{\partial y} + \frac{\partial \tau_{zz}}{\partial z} + \rho_{slag}\, g \qquad [3]$$

In the horizontal direction, the internal pressure (P) is assumed to equal the ferrostatic pressure, which is transmitted directly across the steel shell, so:

$$\frac{\partial P}{\partial z} = \rho_{steel}\, g \qquad [4]$$

This is reasonable everywhere except near the corners that support themselves and near the meniscus where pressure fluctuates. Thus, this model is appropriate within most of the gap over the unsupported wide faces of the slab casting.

In Eq. [3], $V_y\, \partial V_z/\partial y$ and $\partial \tau_{yz}/\partial y$ can be neglected, because $V_y = 0$. The three terms $\rho_{slag}\, V_x\, \partial V_z/\partial y$, $\rho_{slag} V_z\, \partial V_z/\partial z$, and $\partial \tau_{zz}/\partial z$ are shown to be negligible in the next section for typical continuous casting conditions. Thus Eq. [3] simplifies to the following, as gravity and downward viscous drag by the steel shell must balance the upward squeezing from the ferrostatic pressure:

$$\rho_{slag} \cdot \frac{\partial V_z}{\partial t} = \frac{\partial \tau_{xz}}{\partial x} + (\rho_{slag} - \rho_{steel})g \qquad [5]$$

Shear stress in the liquid slag layer depends on the velocity gradient at each point across the channel:

$$\tau_{xz} = \mu\frac{\partial V_z}{\partial x} \qquad [6]$$

The temperature-dependent viscosity of the liquid slag is fit to a simple power-law relation, which better represents low-temperature, high-viscosity behavior than a simple Arrhenius equation:[51]

$$\mu = \mu_s \left(\frac{T_s' - T_{fsol}}{T - T_{fsol}}\right)^n \qquad [7]$$

Assuming that the temperature across the liquid-slag-layer thickness is linear gives

$$T = \frac{x}{d_l}\left(T_s' - T_{\text{fsol}}\right) + T_{\text{fsol}} \qquad [8]$$

Substituting Eq. [8] into [7] and replacing the viscosity term in Eq. [6] with this position-dependent viscosity yields

$$\tau_{xz} = \mu_s \frac{d_l^n}{x^n} \frac{\partial V_z}{\partial x} \qquad [9]$$

Differentiating Eq. [9] and substituting into Eq. [5] yields the following momentum equation, governing the velocity distribution in the liquid film:

$$\rho_{\text{slag}} \frac{\partial V_z}{\partial t} = \mu_s \frac{d_l^n}{x^n} \frac{\partial^2 V_z}{\partial x^2} - \mu_s \frac{n d_l^n}{x^{n+1}} \frac{\partial V_z}{\partial x} + (\rho_{\text{slag}} - \rho_{\text{steel}})g \qquad [10]$$

Differentiating Eq. [1] to get the mold velocity (V_m) and assuming that the solid slag is attached to the mold wall, the boundary conditions for the liquid-slag-layer model (Eq. [10]) are:

solid/liquid slag-layer interface:
$$V_z|_{x=0} = V_s = V_m = \pi s f \cdot \cos(2\pi f t) \qquad [11]$$

liquid slag/steel shell interface:
$$V_z|_{x=d_1} = V_c \qquad [12]$$

Neglecting $\partial V_z/\partial t$ and applying the boundary conditions of Eqs. [11] and [12], Eq. [10] can be integrated to obtain the following "pseudotransient" analytical solution:

$$V_z = \frac{-(\rho_{\text{slag}} - \rho_{\text{steel}})g x^{n+2}}{\mu_s (n+2) d_l^n}$$
$$+ \left(\frac{(V_c - V_s)}{d_l} + \frac{(\rho_{\text{slag}} - \rho_{\text{steel}})g d_l}{\mu_s (n+2)}\right) \frac{x^{n+1}}{d_l^n} + V_s \qquad [13]$$

C. Liquid Slag Layer Flow-Model Validation

To check the validity of the assumptions made to obtain Eq. [13], a fully transient numerical solution was obtained using an explicit finite-difference discretization of Eq. [10] with a central-difference scheme:

$$V_z^{i(t+\Delta t)} = V_z^{i(t)} + \frac{\Delta t}{\rho_{\text{slag}}} \left(\mu_s \frac{d_l^n}{x^n} \frac{V_z^{i+1(t)} - 2V_z^{i(t)} + V_z^{i-1(t)}}{\Delta x^2} \right.$$
$$\left. - \mu_s \frac{n d_l^n}{x^{n+1}} \frac{V_z^{i+1(t)} - V_z^{i-1(t)}}{\Delta x} + (\rho_{\text{slag}} - \rho_{\text{steel}})g \right) \qquad [14]$$

A MATLAB[55] program was coded to solve this equation with the boundary conditions of Eqs. [11] and [12] at different z distances. Table II gives the parameters of four cases used in the MATLAB program. Cases a and b are based on heat-transfer results for typical casting conditions as shown in Table I; cases c and d use an extremely thick liquid layer (2 mm), based on Chavez's work.[47] Discretizing the continuity equation (Eq. [2]) and processing the results at different z distances (specifically, $z = 53$ and 54 mm for case b) allows computations of the other terms in Eq. [3]. Table III shows values of the different terms in Eq. [3] for case b at $t = 0.18$s seconds and $x = 0.16$ mm. Note that $\rho_{\text{slag}}V_x \, \partial V_z/\partial x$, $\rho_{\text{slag}}V_z \, \partial V_z/\partial z$, and $\partial \tau_{zz}/\partial z$ are

negligible compared to the other terms. Also note that the transient term $\rho_{\text{slag}} \, \partial V_z/\partial t$ contributes less than 1.5 pct and, so, can justifiably be neglected too.

Figures 4(a) through (d) show typical velocity profiles computed with these models. For a constant viscosity and a thin liquid layer (Figure 4(a)), the velocity profiles are linear. Otherwise, nonlinearity is significant. Figure 4 also compares the numerical solution and the pseudotransient analytical solution. It shows that the transient effect is negligible for a film thickness of 0.2 mm. Even for an extreme case, a 2-mm-thick liquid film (Figures 4(c) and (d)), the maximum transient effect is barely perceptible. Therefore, the pseudotransient analytical solution to the liquid-slag-layer flow equation (Eq. [13]) is a reasonable approximation of the full transient solution.

Substituting Eq. [13] into [9] gives

$$\tau_{xz} = \frac{(n+1)\mu_s (V_c - V_s)}{d_l}$$
$$+ \frac{(\rho_{\text{slag}} - \rho_{\text{steel}}) g ((n+1) d_l - (n+2)x)}{n+2} \qquad [15]$$

Evaluating Eq. [15] at $x = d_l$ gives the shear stress at the slag/steel interface when a liquid slag layer is present:

$$\tau_{\text{liquid flux/steel}} = \mu_s \frac{(n+1)(V_c - V_s)}{d_l} - \frac{(\rho_{\text{slag}} - \rho_{\text{steel}}) g d_l}{(n+2)} \qquad [16]$$

D. Solid Slag Layer Stress Model

Near the meniscus, the solid slag layer attaches to the mold wall and oscillates with the mold. However, if the solid slag layer breaks, and where it breaks, could greatly affect heat transfer across the gap. A stress model is developed to investigate force balances and possible fracture in the solid slag layer.

The equilibrium force balance in the axial z direction is

$$\frac{\partial \tau_{xz}}{\partial x} + \frac{\partial \sigma_z}{\partial z} + F_z = 0 \qquad [17]$$

Knowing that body forces (F_z) are negligible in the solid layer, Figure 5 illustrates the force balance in a solid-slag-layer discretization element cut from Figure 1 for four typical cases. Evaluating τ_{xz} in Eq. [15] at $x = 0$ gives the shear-stress boundary condition at the interface between the liquid and solid slag layers:

$$\tau_{s/l} = \mu_s \frac{(n+1)(V_c - V_s(t))}{d_l}$$
$$+ \frac{(n+1)}{(n+2)}(\rho_{\text{slag}} - \rho_{\text{steel}})g d_l \qquad [18]$$

Note that this shear stress varies greatly during the oscillation cycle.

The maximum shear stress transmitted to the mold by Coulomb friction with the solid slag layer, due to relative motion of the mold and shell, is

$$\tau_{\max} = \phi_{\text{static}} \cdot \sigma_x \qquad [19]$$

Carbon content	C pct	0.05	pct
Liquidus temperature	T_{liq}	1529	°C
Solidus temperature	T_{sol}	1509	°C
Steel density	ρ_{steel}	7400	kg/m²
Fraction solid for shell thickness location	f_s	0.3	—
Mold powder solidification temperature	T_{fsol}	950	°C
Mold powder viscosity at 1300 °C	μ_{1300}	4.3	poise
Exponent for temperature dependence of viscosity	n	1.6	—
Slag density	ρ_{slag}	2500	kg/m³
Mold powder conductivity	k_{solid}, k_{liquid}	1.5, 1.5	W/mK
Poisson's ratio of slag	ν	0.17	—
Mold slag consumption rate	Q_{slag}	0.41	kg/m²
Mold slag lubrication consumption rate	Q_{lub}	0.2	kg/m²
Solid layer/mold interface friction coefficient	$\phi_{static}, \phi_{moving}$	0.4, 0.4	—
Solid slag layer velocity	V_s	0.	m/s
Casting speed	V_c	1.0	m/min
Pour temperature	T_{pour}	1550	°C
Slab geometry	$W \times N$	1500 × 230	mm × mm
Working mold length	Z_{mold}	800	mm
Oscillation mark geometry	$d_{mark} \times w_{mark}$	0.45 × 4.5	mm × mm
Mold oscillation frequency	f	83.3	cpm
Oscillation stroke	s	7.8	mm
Negative strip ratio of velocity	NS pct	0.3	—
Liquid slag pool depth	h_0	10	mm
Time step	dt	0.002	s
Mesh size	dx	0.5	mm

	Case (a)	Case (b)	Case (c)	Case (d)	
Temperature-dependent viscosity exponent, n:	0	1.6	0	1.6	—
Liquid film thickness, dl:	0.2		2.0		mm
Viscosity at shell surface side, μ_s:	0.53		0.50		Pa
Density, ρ_{slag}:	2500		4000		kg/m³
Casting speed, V_c:	1.0		1.5		m/min
Mold oscillation stroke, s:	7.8		20		mm
Mold oscillation frequency, f:	1.389		1.5		cps
Steel density, ρ_{steel}:	7400		7400		kg/m³
Time-step, Δt:		5.0×10^{-7}			s
Mesh size, Δx:		0.04			mm

$\rho_{slag} \cdot V_z \cdot \dfrac{\partial V_z}{\partial z}$	$\rho_{slag} \cdot V_y \cdot \dfrac{\partial V_z}{\partial y}$	$\rho_{slag} \cdot V_z \cdot \dfrac{\partial V_z}{\partial z}$	$(\rho_{slag} - \rho_{steel}) \cdot g$	$\dfrac{\partial \tau_{yz}}{\partial y}$	$\dfrac{\partial \tau_{zz}}{\partial z}$
−335.	0.0304	0.0431	−48,020.	47,683.	−1.0624

The normal stress (σ_x) comes from the liquid steel ferrostatic pressure and the liquid slag pool above the meniscus, which generates a tiny additional head:

$$\sigma_x = -(\rho_{slag}\, g h_0 + \rho_{steel}\, g z) \qquad [20]$$

Shear stress must be continuous across the gap, including both the boundaries at the mold and steel shell surfaces. When the liquid layer/steel interface shear stress is smaller than the maximum solid-contact shear stress, then the friction force drops to match it, as shown in Figure 5(a). In this "liquid-shear-stress-limited" case (Figure 5(a)), the friction force is less than the maximum possible static friction given in Eq. [19]. Ferrostatic pressure then generates axial stress (σ_z) in the solid layer that is compressive:

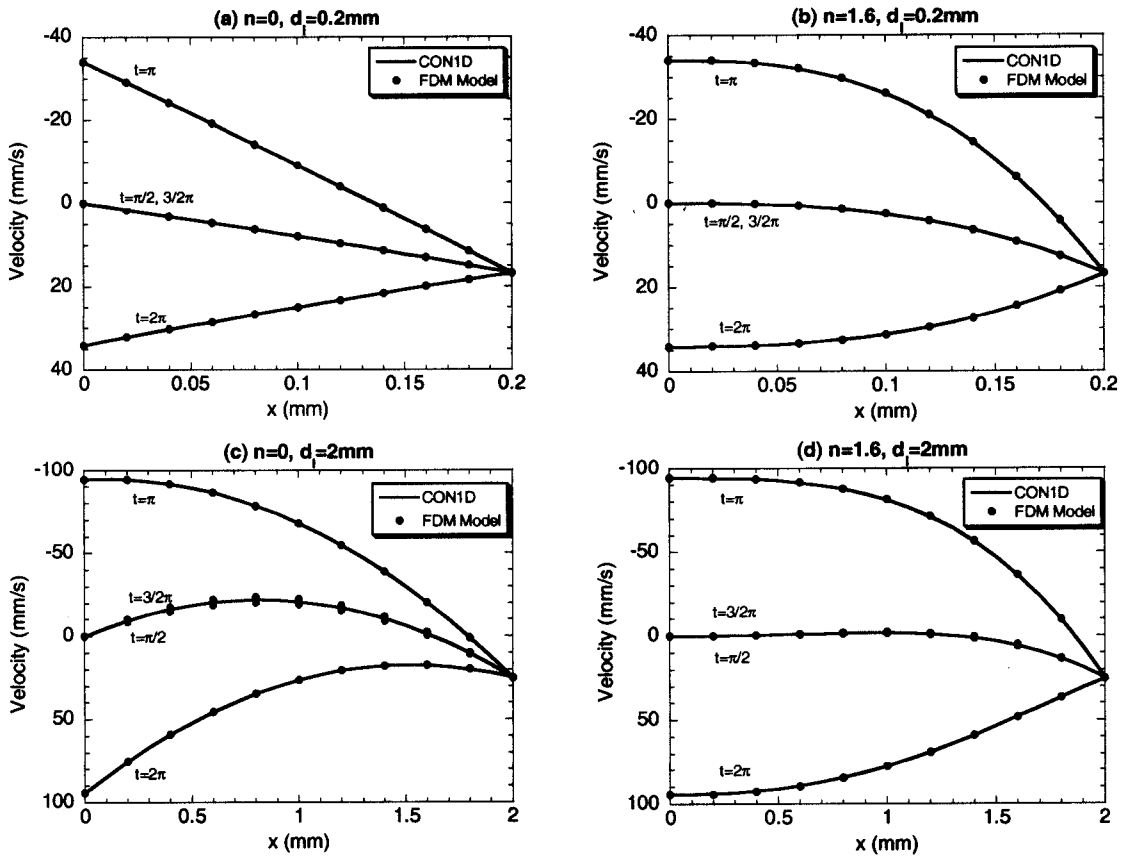$$\sigma_z = -\frac{\nu}{1 - \nu}\, \sigma_x \qquad [21]$$

Fig. 4—(a) through (d) Velocity profiles in liquid flux layer (for different viscosity exponent (0/1.6) and film thickness (0.2/2 mm)).

so, the xz shear stress at the mold side can be calculated from Eqs. [17], [20], and [21] as follows:

$$\tau_{\text{mold}} = -\int_{x=0}^{d_s} d\sigma_z/dz \cdot dx + \tau_{s/l} \qquad [22]$$
$$= \frac{\nu}{1-\nu} \rho_{\text{steel}} \, g d_s + \tau_{s/l}$$

Alternatively, if the liquid-layer shear stress is larger than the maximum static friction, ($\tau_{\text{mold}} = \tau_{\text{max}}$), then axial stress develops in the solid layer to compensate. In order to satisfy the force balance of Eq. [17],

$$d\sigma_z = -d\tau_{xz} \cdot dz / dx \qquad [23]$$

Discretizing Eq. [23] axially and integrating across the thickness, the axial stress in the solid slag layer at $z + \Delta z$ is

$$\sigma_{z+\Delta z} = \sigma_z - \frac{\tau_{\text{max}} - \tau_{s/l}}{d_s} \Delta z \qquad [24]$$

Specifically, axial stress is tensile during the upstroke and compressive in the downstroke for this "mold-friction-limited" case, shown in Figure 5(b). Furthermore, the axial tension accumulates over successive slices of the solid slag layer. The shear stress transmitted to the mold wall is the minimum of the maximum static-friction stress and the solid/liquid interface stress:

$$\tau_{\text{mold}} = \min\left(\frac{\nu}{1-\nu} \rho_{\text{steel}} \, g d_s + \tau_{s/l}, \tau_{\text{max}} \right) \qquad [25]$$

E. Solid Slag Layer Stress-Model Validation

To validate the stress model of the solid slag layer, a simplified case was solved using elastic finite-element stress analysis with ANSYS.[56] Figure 6 shows the ANSYS model domain and mesh. The boundary condition at the mold side had displacements fixed to zero; that at the liquid side was the normal ferrostatic pressure (σ_x) from Eq. [20] and the tangential shear stress $\tau_{s/l}$ (from CON1D). Table I gives the input conditions and simulation parameters used in CON1D. Figure 7 compares the stress results from ANSYS and CON1D using Eqs. [24] and [25]. The CON1D model matches ANSYS except within 10 mm near mold exit, where the real axial stress must quickly tend to zero (to match ambient atmospheric pressure).

F. Solid Slag Layer Fracture Model

If the axial stress exceeds the fracture strength, the solid slag layer will break and be dragged down the mold wall. The shear stress on the mold/slag interface for this condition is

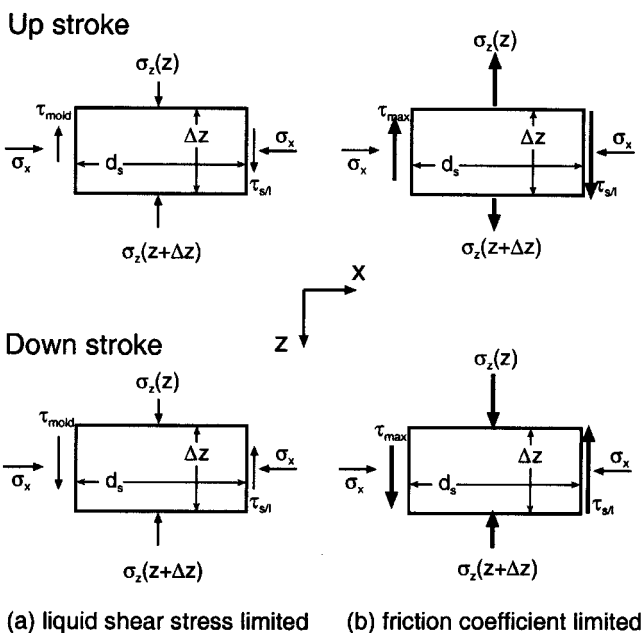$$\tau_{\text{mold}} = \phi_{\text{moving}} \cdot \sigma_x \qquad [26]$$

Fig. 5—(a) and (b) Force balance on solid slag layer section.

Fig. 6—ANSYS solid slag stress model domain, mesh, and BCs.

Substituting Eqs. [18] and [26] into Eq. [22] can solve for the solid-layer velocity after it detaches from the mold wall. Fracture and sliding of the solid slag layer tend to create a gap between the upper attached solid layer and the lower moving layer. This gap may refill with liquid slag, and the solid layer might reattach to the mold wall when the instantaneous velocity of the oscillating mold wall equals the moving solid slag layer velocity. The time for the liquid slag to fill the gap and the solid slag to reattach depends on the slag consumption rate and liquid-slag fluidity. The fracture and filling process requires extra slag consumption, which decreases the liquid-layer thickness and increases shear stress(/friction) for the whole mold.

G. Mold Friction

The friction measured in operating casting molds may come from mold/slag contact, an excessive taper, misalignment, or a combination of the three.

1. Slag-layer friction

Previous research has suggested that friction against the slag layer is important.[57] The liquid-slag-layer flow model and solid-slag-layer stress model described in this work give the shear stress on the mold wall (τ_{mold}) due to mold/slag contact. Integrating the shear stress over the mold face gives the total friction force due to contact between the mold and slag layers:

$$F_{contact} = \int_0^{Z_{mold}} \tau_{mold} \cdot 2\,(W + N) \cdot dz \qquad [27]$$

where Z_{mold} is the working mold length, W is the slab width, and N is the slab thickness.

This model has been incorporated into CON1D and is used for the study described in Sections III and IV.
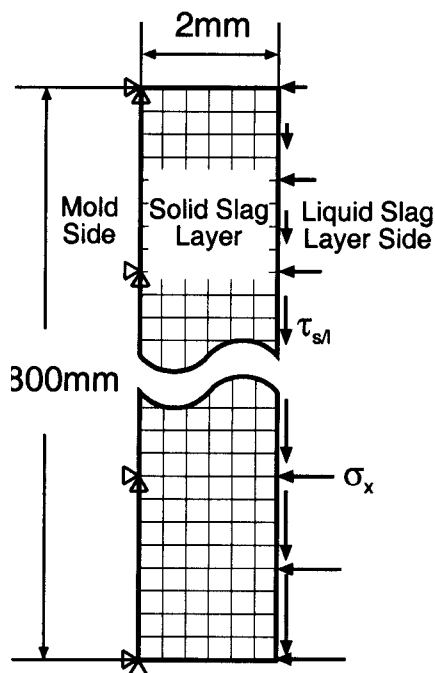
2. Excessive taper

If the solid slag layer remains attached to the mold wall all the way down the mold, there will be a continuous, thick liquid slag layer (to provide slag consumption) and a thick solid slag layer, leading to low heat transfer across the mold/shell gap. Then, the shell will have a relatively high surface temperature and small shrinkage. In this case, an excessively narrow face taper may squeeze the steel shell and, therefore, lead to increased friction. The maximum force from squeezing the shell occurs if the shell buckles, leading to longitudinal surface depressions, such as off-corner gutter in extreme cases,[13] as shown in Figure 8. Applying the Eular critical-buckling-load equation with rigid ends yields an estimate of the normal stress on the mold wall (F_{cr}):

$$F_{cr} = \frac{4\pi^2\,EI}{L_{eff}^2} = \frac{4\pi^2\,E}{L_{eff}^2}\,\frac{b^3 h}{12} \qquad [28]$$

Where b is the shell thickness, h is the vertical contact length along the narrow face, L_{eff} is the unsupported shell width across the wide face from the corner, and E is the effective elastic modulus of the hot steel shell. So, the friction due to buckling for each narrow face is

$$F_{excessive\ taper} = 2\phi_{static} \cdot F_{cr} \qquad [29]$$

3. Misalignment friction

Misalignment of the mold and strand is another important potential cause of friction. The friction force during each oscillation cycle is inferred from the difference between the force-transducer measurements with and without molten steel in the mold.[58] Currently, such friction signals can be used to monitor and detect misalignment problems in operating casters.
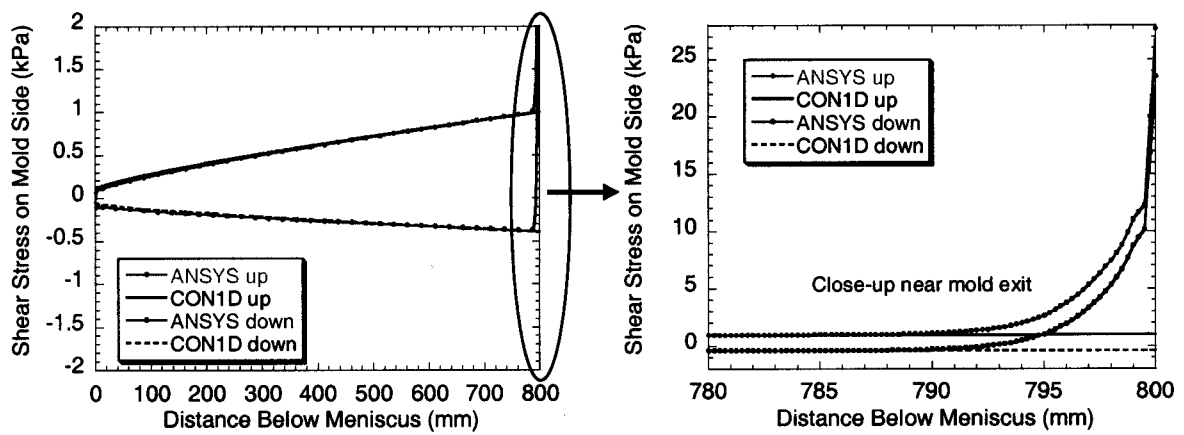
(a) Shear stress on mold side
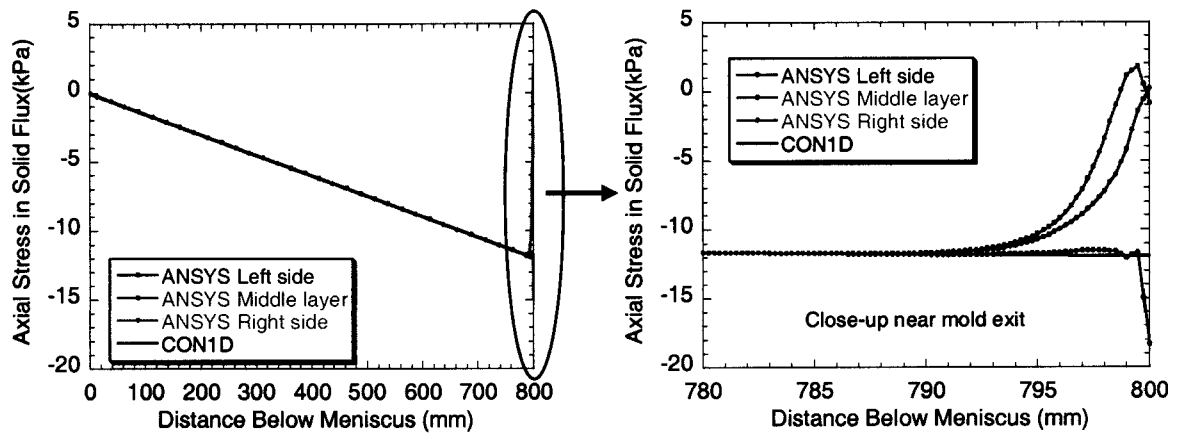
(b) Axial stress in solid slag

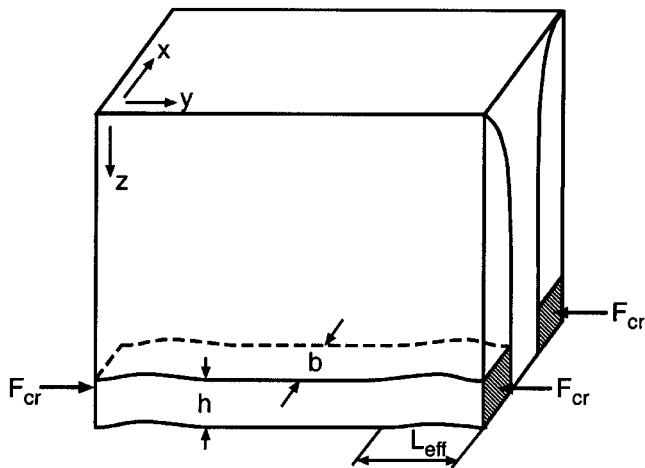Fig. 7—(*a*) and (*b*) Comparison of CON1D and ANSYS results (case 1a).

Fig. 8—Schematic of friction forces from excessive taper of narrow mold faces.

III. EXAMPLE APPLICATION

The CON1D model is first used to simulate behavior for the typical casting conditions listed in Table I. During casting, mold slag may absorb reoxidation products such as alumina. This changes the slag composition and its properties. Alumina tends to decrease slag basicity,[52] which decreases the crystallization temperature[52,59,60] and increases viscosity at high temperatures.[52,59–61] This makes the slag easier to be glassy.[59,62] Figure 9 shows the viscosity curves *vs* temperature assumed for three slags, which were chosen to match with slag viscosity data measured by Lanyi and Rosa.[52] The typical continuous-cast slag A might be crystalline or glassy (slag A2 in Lanyi and Rosa[52]); slag C is readily crystalline (slag A6 in Lanyi and Rosa[52]). Slag G is slag C with 25 pct additional alumina, which has a high tendency to be glassy.[52] The composition and properties of these three slags are listed in Table IV.

Computation of both heat transfer and friction depends greatly on the total consumption rate of slag into the gap (Q_{slag} (kg/m^2)), which is an input parameter in this work. It is important to introduce the concept of "lubricating consumption rate" (Q_{lub}), which is the slag consumption not carried inside the oscillation marks:

$$Q_{lub} = Q_{slag} - Q_{osc} \qquad [30]$$

where is Q_{osc} is the consumption rate of slag carried within the filled oscillation marks, found from

$$Q_{osc} = 0.5\rho \cdot d_{mark} \cdot w_{mark} / L_{pitch} \qquad [31]$$
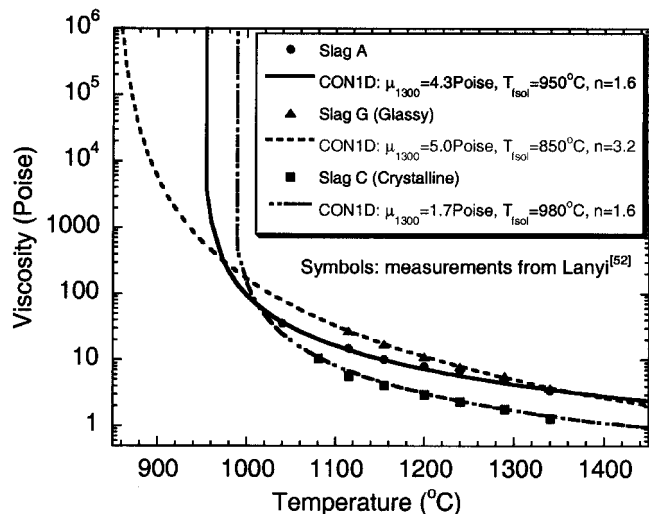
The liquid slag represented by Q_{lub} acts to lubricate the mold-shell interface and, thereby, lower friction. The CON1D model is run with different mold slags, consumption rates, and casting speeds to study the effect of mold powder properties and oscillation practice. The related parameters are listed in Tables IV through VI.

A. *Typical Results*

Simulations were first run for typical low-friction conditions (case I (Table I)), assuming that all solid slag is attached to the mold wall and there is a constant lubrication consumption rate of 0.2 kg/m^2. At a 1.0 m/min casting speed, the total consumption rate (Q_{slag}) is 0.41 kg/m^2. Figure 10 shows typical results with slag A. The mean heat flux in the mold is 1.24 MW/m^2, and the shell thickness is 20.4 mm at mold exit (based on a solid fraction of 0.3). A uniform liquid slag layer of 0.29 mm is predicted (Figure 10(d)), while the solid layer continually increases down the mold. Such a thick solid layer could build up over time, starting during initial mold filling with starter slag. Once it reaches steady state, it does not consume any new mold powder. Increasing the casting speed is naturally predicted to raise the heat flux but lower shell growth.

Figure 11 shows the cooling history of various points in the slag layer for case I with slags A and G. The superimposed TTT curve of a conventional industrial mold slag (7.9 pct Al$_2$O$_3$)[63] is used to estimate the onset of crystallization for slag A. Figure 11(a) predicts crystallization in most of the slag layer (including the oscillation marks), except for the very thin (0.2 mm) layer adjacent to the mold wall, which is quenched rapidly and remains glassy. Extra alumina in the slag delays the onset of crystallization and increases the temperature range of crystallization, so the
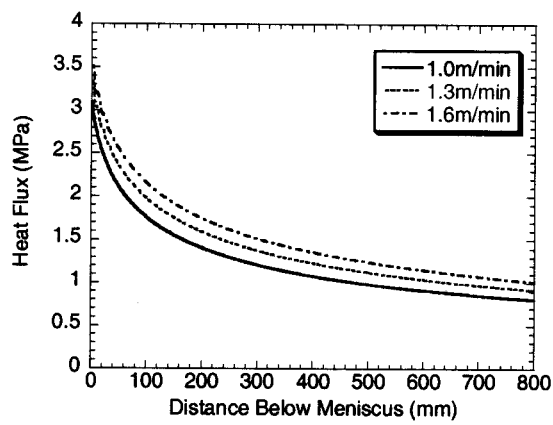

Fig. 9—Mold slag viscosities modeled in this work.

Table IV. Slag Composition and Properties

Slag	CaO (Wt Pct)	SiO$_2$ (Wt Pct)	Al$_2$O$_3$ (Wt Pct)	MgO (Wt Pct)	Na$_2$O (Wt Pct)	K$_2$O (Wt Pct)	F$_2$ (Wt Pct)	FeO (Wt Pct)	MnO (Wt Pct)	B$_2$O$_3$ (Wt Pct)	T_{fsol} (°C)	n (—)	μ_{1300} (P)
A	32.3	36.4	8.9	0.7	5.0	1.9	8.3	3.0	—	3.4	950	1.6	4.3
G	27.5	30.3	21.4	0.9	5.6	—	12.0	1.1	1.3	—	850	3.2	5.0
C	34.8	38.3	0.5	1.2	7.1		15.2	1.4	1.6		980	1.6	1.7

Table V. Case Study Parameters

Slag Parameter	Case I	Case II	Case III
Lubrication consumption, Q_{lub}:	0.2 kg/m^2	critical	0.2 kg/m^2
Solid layer status:	attached	attached	moving

Table VI. Mold Oscillation Practice with Casting Speed

| Casting Speed, V_c (m/min)	Oscillation frequency, f (cpm)	Negative Strip Time, NST (s)	Negative Strip Ratio, NS Pct (—)	Oscillation Mark, $d_{mark} \times w_{mark}$ (mm × mm)	Oscillation Marks Consumption, Q_{osc} (kg/m^2)
1.0	83.3	0.24	0.3	0.45 × 4.5	0.21
1.3	108.3	0.19	0.3	0.30 × 3.0	0.094
1.6	133.3	0.15	0.3	0.16 × 1.6	0.027
2.0	166.7	0.12	0.3	0 × 0	0
3.0	250.0	0.08	0.3	0 × 0	0
5.0	416.7	0.05	0.3	0 × 0	0

(a) Heat Flux
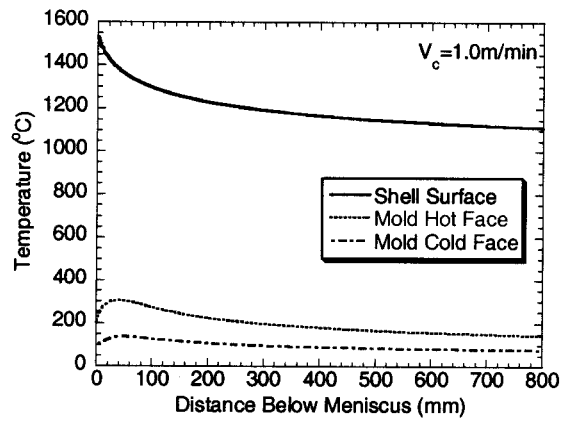
(b) Shell and Mold Temperature
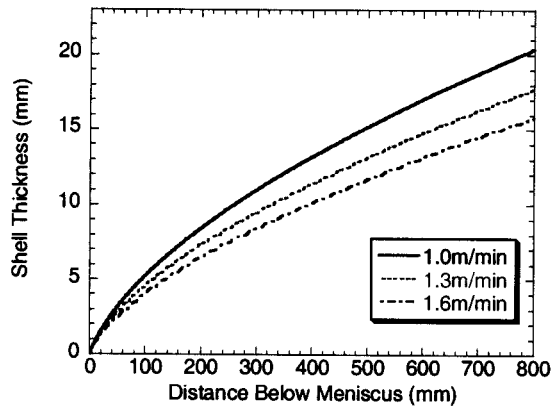
(c) Steel Shell Thickness
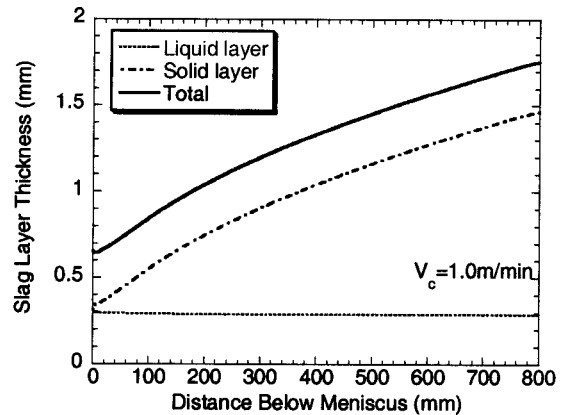
(d) Slag Layer Thickness

Fig. 10—(a) through (d) Typical results of case I with slag A.

TTT curve of a slag with 19.5 pct Al_2O_3[64] is used to estimate the onset of crystallization for slag G. Figure 11(b) shows that no points within slag G cross the TTT curve, so no crystalline phase is predicted. This agrees with the assumption that slag G tends to be glassy.

The shear stress and axial stress along the solid slag layer were plotted in Figure 7. It shows that the solid slag layer is in compression almost everywhere. Therefore, the attached solid slag layer is stable and no fracture should occur. This can happen in practice, as evidenced by the recovery of a solid slag layer attached to the mold wall after 1 hour of casting, which contains trace elements only found in the starter slag (consumed in the first few minutes).[65,66] The accompanying stable, thick liquid layer ensures a very low friction force on the mold wall.

Figure 12(a) predicts the slag-layer thicknesses of the glassy and crystalline slags, assuming the same consumption rate and other conditions (Table I). The glassy slag G is thinner due to its lower solidification temperature. Therefore, it produces a slightly higher heat flux and lower shell temperature than the crystalline slag, as shown in Figures 12(b) and (c). If the lower consumption rate that generally accompanies higher-viscosity slags in a real caster[67,68] were taken into account, these differences would be even greater. In either case, this prediction matches well-known measured behavior.[25,68,69]

Note that the crystalline slag is predicted to have lower friction on the mold wall (Figure 12(d)). This is mainly because of its lower viscosity gradient at high temperature (Figure 9), which helps the solid crystalline layer to stay attached to the mold wall and prevent fracture.

B. Critical Slag Consumption Rate

A lower slag consumption rate (Q_{lub}) leads to higher shear stress at the liquid/solid slag interface. If friction on the mold side cannot balance the shear stress along the solid/liquid interface, axial tensile stress must build up in the solid slag layer to compensate. When axial stress in the solid slag exceeds the slag fracture strength, the solid slag breaks and is dragged down the mold wall. The critical consumption rate is the minimum consumption rate needed to keep solid slag attached to the mold wall without breaking or sliding. In order to find it, the complete CONID model was run several times with different consumption rates (case II), assuming a slag fracture strength of 80 MPa.[70] Figure 13 shows the axial-stress and shear-stress distribution of slags A and G along the mold wall at their corresponding critical consumption rates. It shows that tensile axial stress accumulates in the solid slag only when liquid shear stress exceeds the maximum static solid friction. In each case,
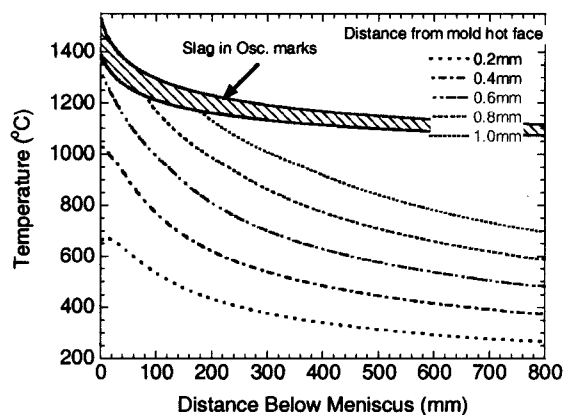
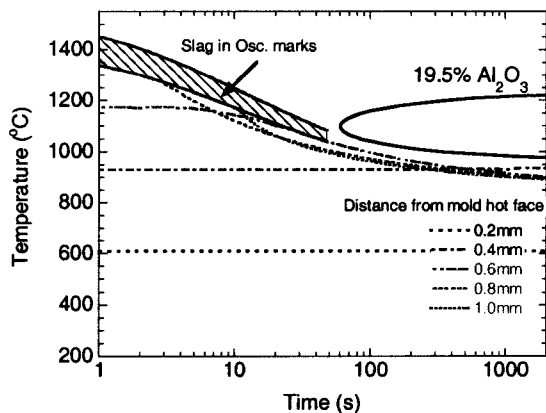**(a) Slag A (Crystalline)**
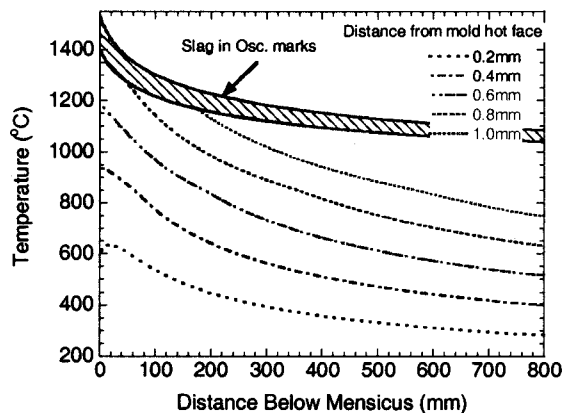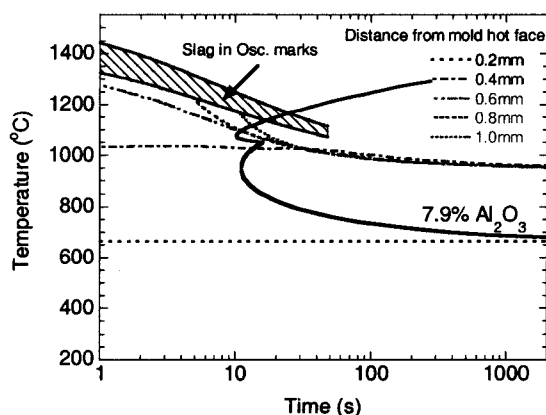
(b) Slag G (Glassy)

Fig. 11—(a) and (b) Slag layer cooling history with TTT curves.

fracture is predicted during the upstroke when axial stress just exceeds the slag fracture strength. All stresses are compressive during the downstroke.

Slag G has a 60 pct larger critical lubricating consumption rate than slag A (0.12 vs respectively). 0.075 kg/m², slag C has similar behavior to slag A, but with an even lower critical Q_{lub} value: 0.05 kg/m². It confirms the general observations that crystalline slags are more stable than glassy slags. Combined with their thicker layer and lower heat flux, this may explain why such crystalline slags are better for depression-and crack-sensitive steel grades.[7,69]

Another important difference between slags A/C and G is the position of slag fracture. As the consumption rate lowers, the glassy slag drops below the critical consumption rate first and fractures first near the mold exit. For the crystalline slags A and C, the solid slag layer fractures within 100 mm near the meniscus. These results show that the sharpness of the slag-viscosity increase near the solidification temperature is more important than the popular slag property of slag viscosity at 1300 °C.

Figure 14 shows the heat flux and mold temperature of these two critical cases. Relative to case I, very high heat flux is predicted near the meniscus. This is also indicated by the high mold temperature at that region. This also implies that in a real caster, if an abnormally high mold temperature is observed near the meniscus, it may be due

to a temporary consumption-rate drop, regardless of slag type. This should also correlate with solid slag breaking and moving down the mold wall. Slag fracture, in turn, will cause temporary gaps, heat-flux drops, and thermal stresses in the shell. The phenomena of a high meniscus heat flux and high variations are known to correlate with strand defects,[11,12] which is consistent with the model prediction here.

C. Mold Friction

1. Attached slag layer

When casting with a stable conventional consumption rate ($Q_{slag} = 0.41$ kg/m²), the model predicts a stable solid slag layer and a very low friction force. For the cases studied here, the mold-wall shear-stress amplitude is 0.85 MPa for slag A and 2.52 MPa for slag G, which are far lower than reported measured friction data.[71] The high friction force measured in operating casters likely comes from three possible causes: a moving solid slag layer, excessive taper, or misalignment.

2. Moving solid slag layer

If the liquid slag level at the meniscus varies, it cannot keep a steady flow into the mold/strand gap even if the mold taper and alignment are reasonable and do not contribute to

(a)
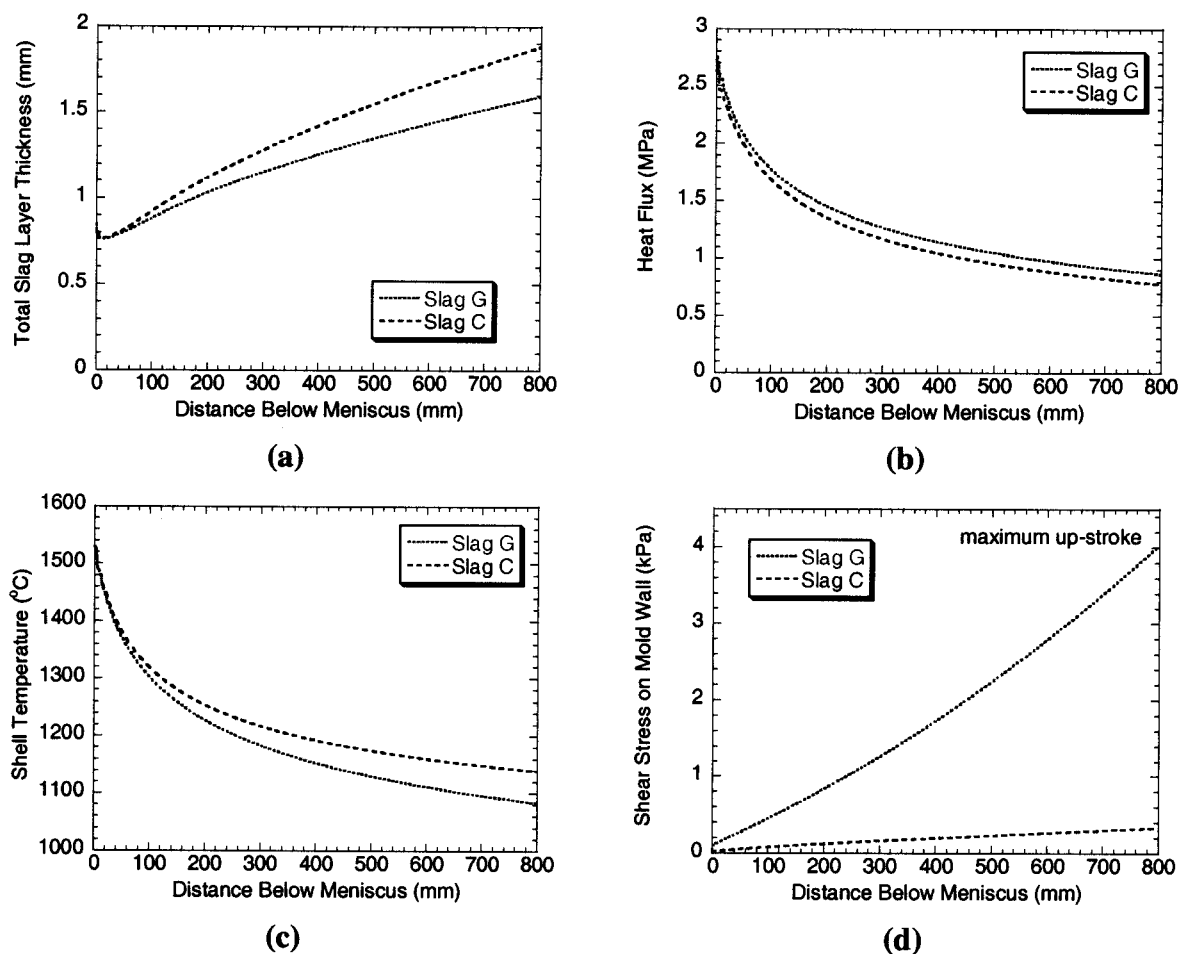
(b)

(c)

(d)

Fig. 12—(a) through (d) Effects of slag type on slag layer thickness, heat flux, and shell temperature friction.

friction. The solid slag layer may break and move along the mold wall, accounting for part of the slag consumption. For a given consumption rate, the liquid slag layer is thinner when the solid layer moves. This leads to higher heat flux and higher friction and, therefore, perpetuates the slag fracture and motion. The fracture position predicted for slag A (case II with a critical consumption rate) is near the meniscus. Thus, the low-viscosity liquid layer may quickly fill in the gap due to facture, and the solid slag layer might reattach to the mold wall until the next fracture. For slag G, if the consumption temporarily drops lower than the critical consumption rate, the solid-slag-layer fracture will occur further above the mold exit.

To model a moving solid slag layer, its average velocity is simply assumed to be some small constant percentage of the casting speed (v_f). In case III, assuming $v_f \approx 5$ pct produces total-friction-force predictions within the measured range of 15 to 23 kPa.[71] Note that the average "moving" solid-slag-layer velocity is actually the time average of a highly transient process, calculated with an intermittent procedure of solid-layer fracture, movement, and reattachment. Most of the time, the solid layer still sticks to the mold wall, so the shear stress can still be calculated based on liquid-layer friction and the maximum static friction between the mold and solid layer. Figure 15 shows that both the liquid

and solid moving layers are thinner than the attached one. In particular, the liquid slag layer gets thinner with distance down the mold and nearly runs out by the mold exit. This increases friction greatly.

3. *Friction variation during an oscillation cycle*
Figure 16(a) shows the mold velocity and casting-speed profile during half of one oscillation cycle. It shows that at one instant (0.24 seconds), the mold velocity equals the casting speed, so there is no shear stress. After that time, the mold moves down faster than the shell during the period of "negative strip." Thus, the stress acting on the slag layer shifts from tension to compression during that instant. It is also seen that the shear stress on the mold wall with a "moving" solid slag layer (Figure 16(c)) is much higher than with an attached layer (Figure 16(b)). The shear stress increases with distance along the mold length, and the transition from tension to compression becomes sharper for a moving layer. In the upper mold, liquid slag controls the friction between the mold and shell, so the shear stress is nearly sinusoidal. In the lower mold region, the solid slag layer controls friction and the shear-stress profile tends toward a square wave.

Figure 17 shows the shear stress down the mold at different times during the oscillation cycle. For all times,
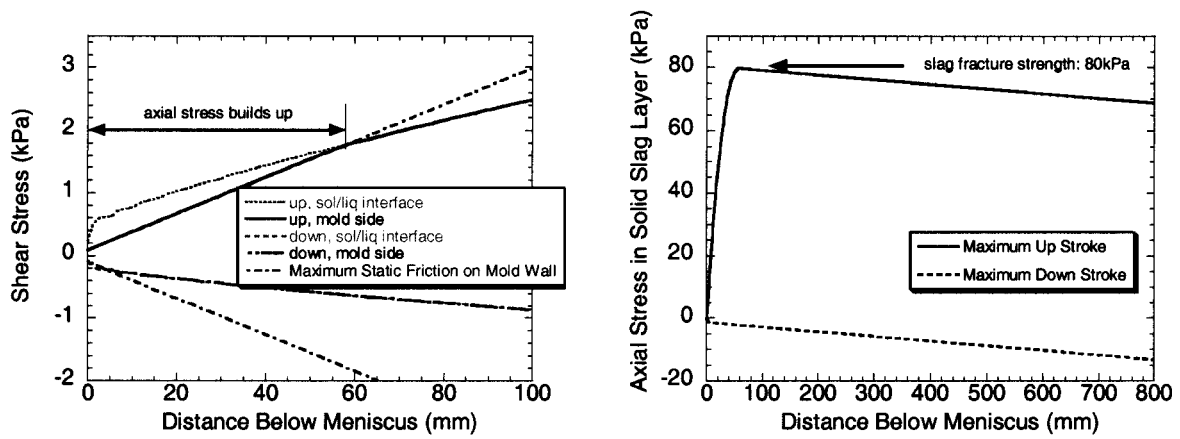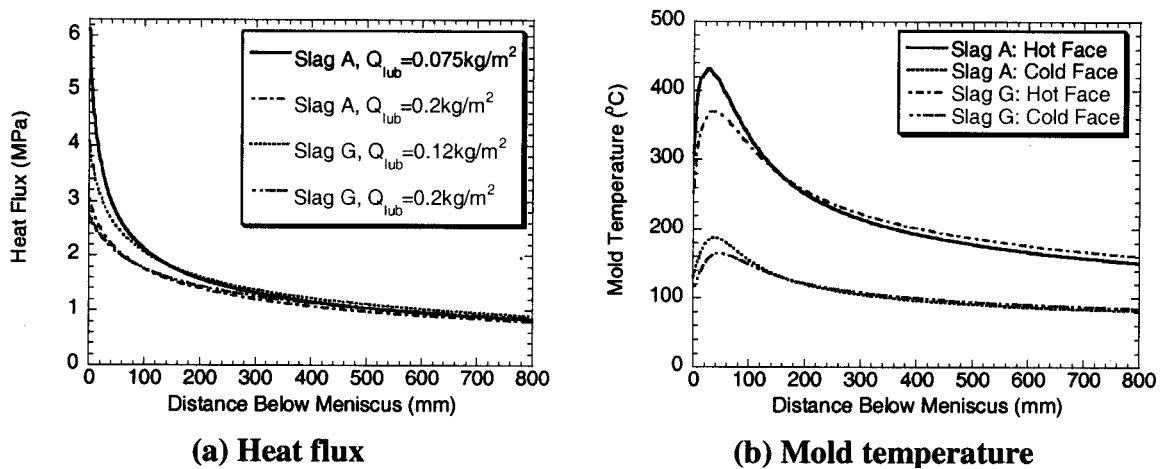
(a) Slag A
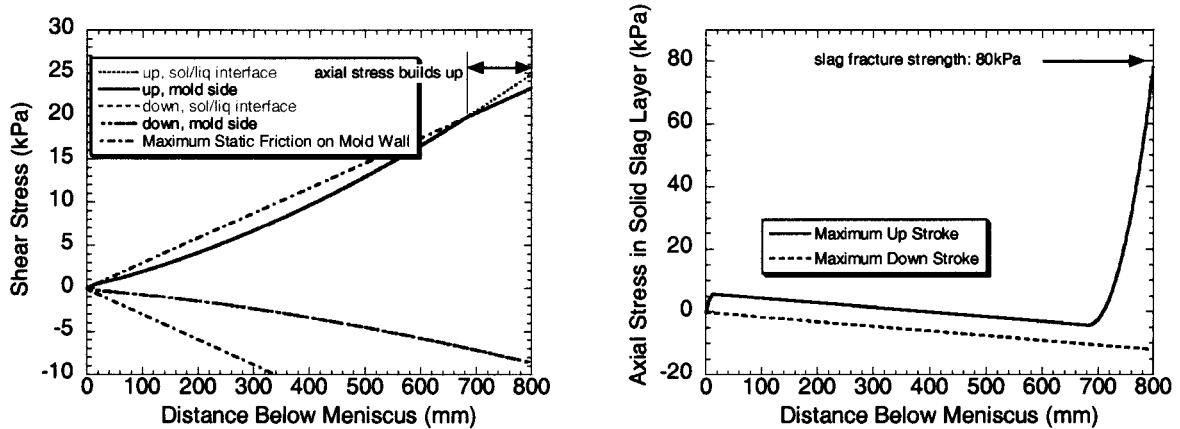
(b) Slag G

Fig. 13—(a) and (b) Effect of slag type on axial stress buildup in solid layer for critical Q_{lub}.

(a) Heat flux

(b) Mold temperature

Fig. 14—(a) and (b) Comparison of heat flux and mold temperature with critical consumption rate.

there is a transition from curved to straight, where liquid-slag-layer control transfers to solid-slag-layer control. The "average" is the mean of the absolute values of all the shear stresses over the whole oscillation cycle and is very near to the curve when V_m is zero. This means that the average

friction force can be estimated with a simple static-mold model. Integrating the shear stress over each mold face at each instant gives the total-friction-force history during each oscillation cycle, as shown in Figure 18 for different cases.
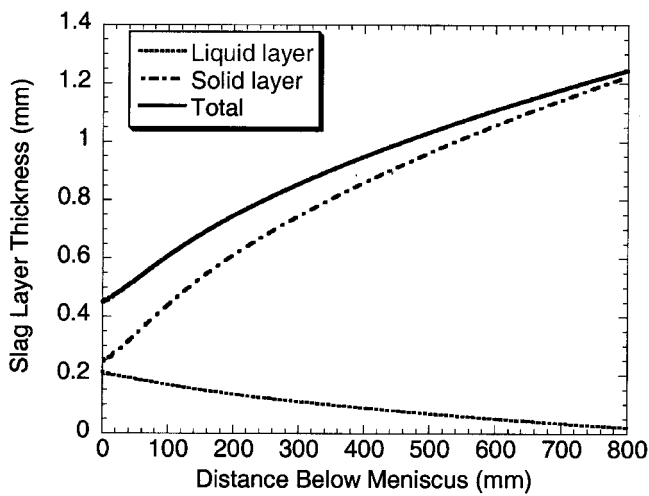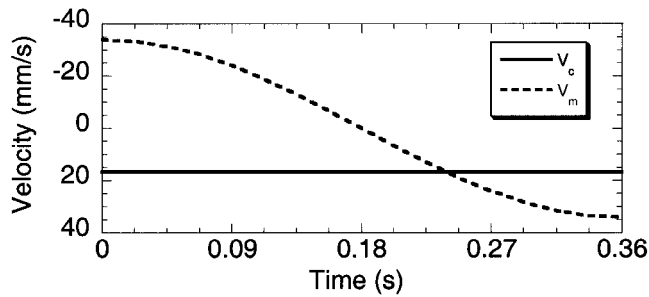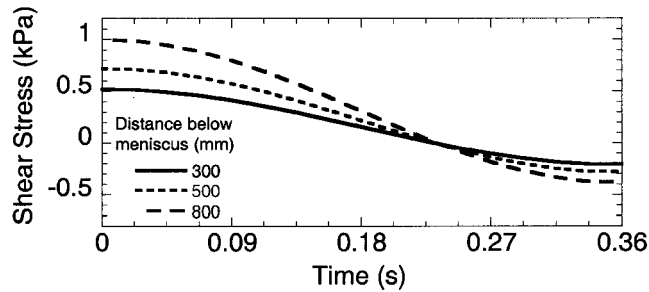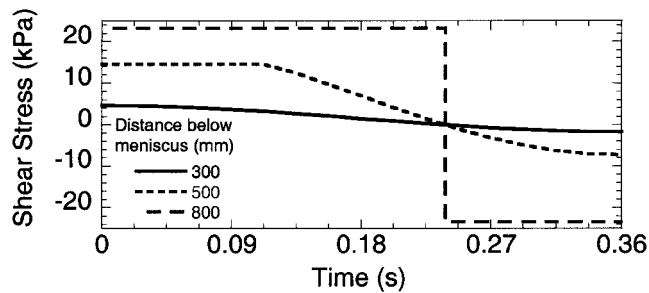
Fig. 15—Slag layer thickness with moving solid layer (slag A).

(a) Casting speed and mold velocity

(b) Attached solid layer (Case I)

(c) "Moving" solid layer (Case III)

Fig. 16—(a) through (c) Velocity and shear stress during half oscillation cycle.
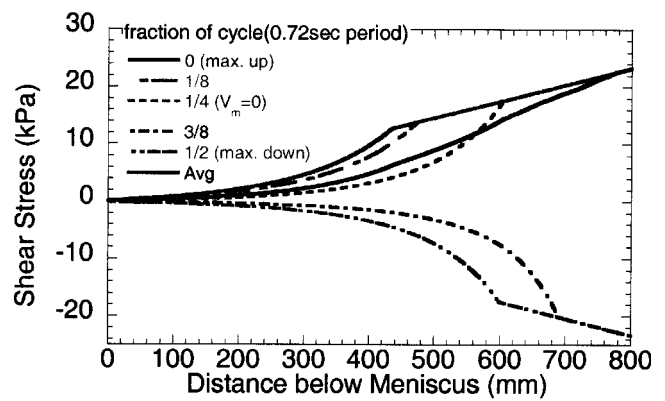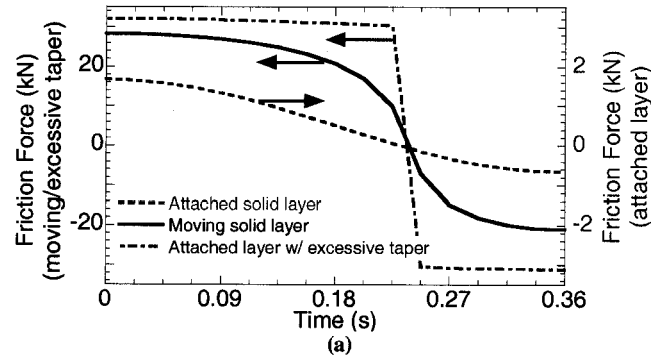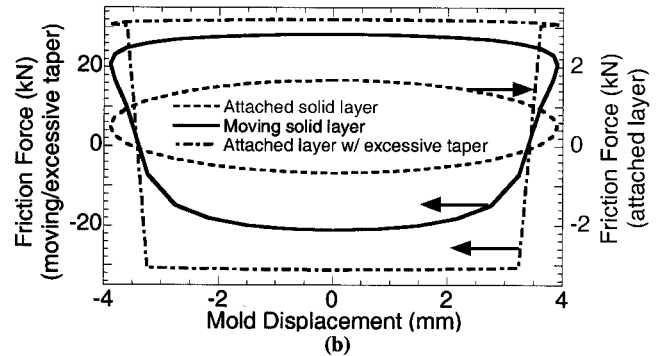

Fig. 17—Shear stress down the mold wall with moving solid layer (slag A).

(a)

(b)

Fig. 18—(a) and (b) Friction force over oscillation cycle (slag A).

4. Total mold friction

Figure 18 shows that the friction due to shear stress is very small if the solid slag layer is attached and there are no other sources of friction. Friction with an intermittent attached solid layer is 10 times larger and has a sharper

transition from tension to compression. Another possible cause of high friction may be squeezing of the steel shell due to an excessively narrow face taper. This is most likely when the shell temperature is high and shrinkage is small at high casting speeds. A rough estimation of the magnitude of this friction is 15 kN on each narrow face, based on Eqs. [28] and [29], assuming that buckling happens over the last 10 mm ($h = 10$ mm) near mold exit, the shell thickness is $b = 20$ mm, $L_{eff} = 600$ mm, and $E = 25$ GPa at 1100 °C. This corresponds to an average friction stress over an 800-mm-long, 230-mm-thick, and 1500-mm-wide slab mold of 10 kPa, which is similar to measured data.[71] Figure 18 shows that the friction force during an oscillation cycle for excessive taper can be identified by its almost-square shape. In contrast, liquid-slag lubrication produces a smooth curve with a very gradual transition. Thus, the lubrication/friction state of the mold can be identified from the shape of the friction-force curve during an oscillation cycle,

in addition to its magnitude. Misalignment-friction curves are expected to be curved according to gradual changes in its extent during the cycle.

IV. CONSUMPTION AND CASTING-SPEED STUDY

A. *Effect of Slag Properties on Critical Consumption Rate*

The most important parameter affecting slag shear stress and fracture was found to be the liquid slag consumption rate. So long as the consumption rate exceeds a minimum critical rate, the slag will not fracture. A parametric study was conducted on the minimum critical consumption to keep a stable attached solid slag layer. Doubling the fracture strength of the crystalline mold slag allows the critical Q_{lub} value for slag A to decrease by only 7 pct and delays the fracture position from 60 to 100 mm below the meniscus. The fracture strength has even less effect for slag G. The effects of the slag's Poisson's ratio, the liquid slag's pool depth, and the mold thickness on the critical consumption rate were negligible.

Maintaining a high mold/slag friction coefficient is important to lowering the critical consumption. As shown in Figure 19, especially for slag G, when the friction coefficient is lower than 0.15, the slag layer can fracture, even for a stable conventional consumption rate.

Oscillation marks act as an extra resistance layer between the liquid slag layer and the steel shell. Thus, they slightly lower the temperature in the liquid layer, which leads to a higher-viscosity liquid, higher shear stress, easier flux fracture, and higher critical consumption. Specifically, 0.45 mm × 4.5 mm oscillation marks cast at 1.0 m/min increase Q_{lub} by 0.01 kg/m^2 for both slags (15 pct for slag A and 9 pct for slag G) relative to cases with no oscillation marks.

B. *Effect of Casting Speed on Critical Consumption Rate*

The influence of casting speed on the mold friction and interface heat flux has been investigated in a parametric study. Based on case I, the casting speed was varied from 1.0 to 5.0 m/min. The stroke was fixed at 7.8 mm, and the oscillation frequency was adjusted to keep a constant negative strip ratio of 0.3 and a constant pitch length of 12 mm. The negative strip time, thereby, decreases with increasing casting speed, so the oscillation-mark depth decreases.[72] The powder consumption rate, thus, decreases due to the shallower oscillation marks and higher oscillation frequency.[73] The oscillation-mark depth becomes negligible when the casting speed is greater than 2 m/min. Table VI gives the mold oscillation parameters used. Those parameters are chosen based on some previous plant measurements of oscillation-mark depth[72] and total mold powder consumption rate,[11,26,75] as shown in Figures 20 and 21.

Figure 21 also compares measured consumption rates[11,26,74,75] with critical consumption rates calculated in this study. The measured consumption rates exceed the critical rates, which indicates that slag fracture should be a rare transient event. If the total consumption rate can be steadily maintained, the strand should be well lubricated and a stable solid slag layer should remain attached to the mold. Figure 21 shows that measured consumption rates decrease with increasing casting speed. When there is significant consumption by the oscillation
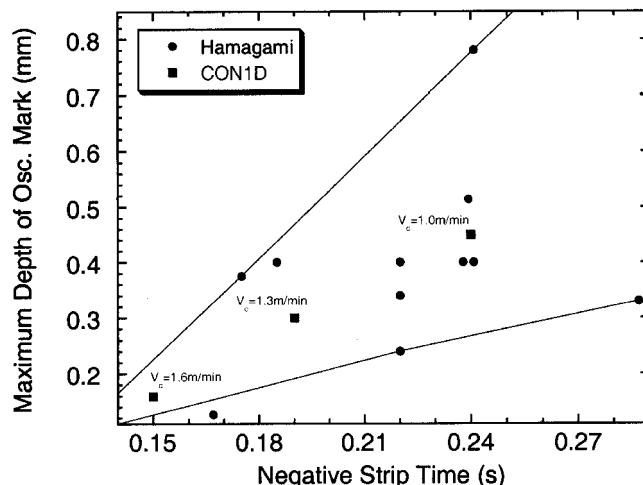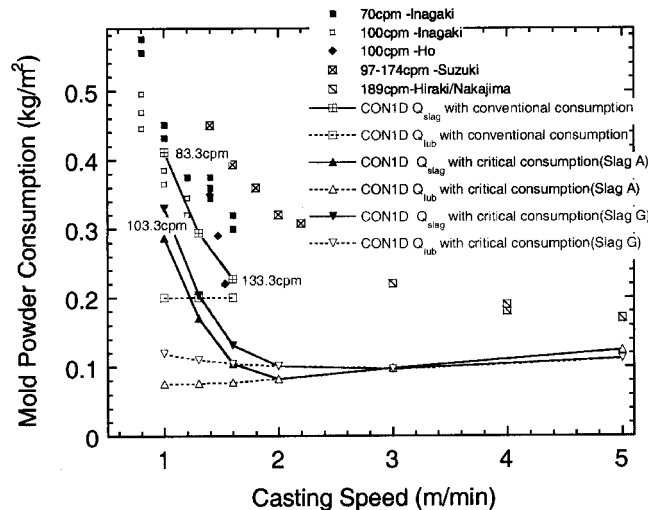
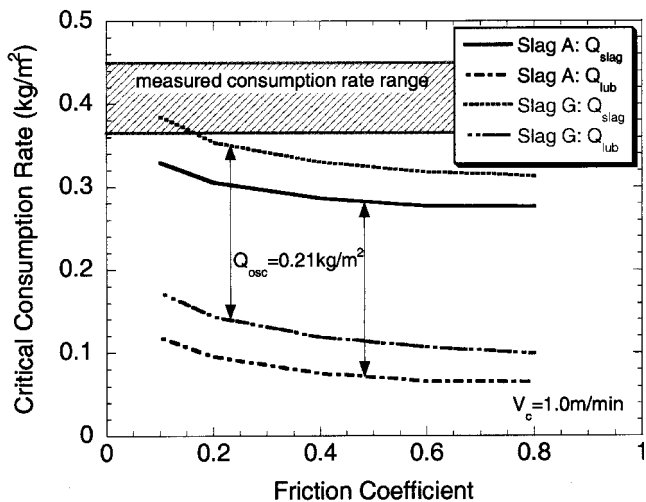Fig. 20—Maximum oscillation marks depth.

Fig. 19—Effect of friction coefficient on critical consumption rate.

Fig. 21—Powder consumption rates.

marks (Q_{osc}), the critical consumption also decreases with increasing casting speed. This is because the oscillation-mark depth decreases, carries less slag, and increases the lubrication-consumption component, thus helping to keep the solid layer attached to the mold wall as explained previously. However, at a higher casting speed (>2 m/min), when the oscillation-mark effect is negligible, the critical consumption rate increases slightly with casting speed.

Figure 22 shows two opposing effects of casting speed on solid slag fracture, excluding oscillation marks and their effects. Increasing the casting speed increases the velocity difference between the mold and shell, which tends to increase friction. It also increases the shell-surface temperature, which tends to decrease slag viscosity and friction. For slag A, the first effect prevails, so the slag always fails near the meniscus, and the higher casting speed is more dangerous to slag fracture. To be specific, increasing V_c from 1.0 to 2.0 m/min requires the critical Q_{lub} to increase by 25 pct. Also, the fracture position occurs closer to the meniscus (moving from 60 to 30 mm). When the critical fracture position is near the mold exit, such as slag G at less than 3.0 m/min, the effect of higher surface temperature predominates, so the higher casting speed helps to avoid slag fracture, as shown in Figure 22(b). Thus, increasing the casting speed from 1.0 to 2.0 m/min decreases critical Q_{lub} by 8 pct. However, further increasing the casting speed above 3.0 m/min causes the critical fracture position to move near the meniscus and increases the critical Q_{lub} as for slag A.

Note that the minimum critical consumption rate occurs at an intermediate speed (~2 m/min) for the conditions of this study, which is the safest speed for slag-layer stability. The measured consumption rates exceed the calculated critical consumption rates by the largest factor (~3 times) for this intermediate speed. Safety margins are less at both the lower speed and higher speed. At the very high speed (~5 m/min), measured consumptions approach critical levels. This indicates that solid slag layer stability becomes a general problem at high speeds (unless consumption or another condition assumed here is changed).

Figure 23 compares the average heat flux with measured and fitted data.[76–79] The average mold heat flux increases with higher casting speed, with lower consumption rate, or with a moving solid slag layer. Note that the average heat flux of the cases with moving slag or with a critical consumption rate (just about to move) almost hit the upper bound of measurements. High and variable heat flux is another indication of slag-layer fracture.
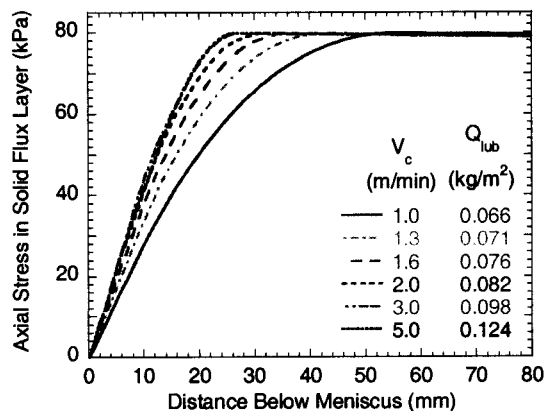
C. *Effect of Casting Speed on Friction Stress*

Finally, CON1D was run with a detached solid slag layer assumed to be moving at an average velocity of 5 pct of the casting speed (case III). The lubrication consumption rate was assumed to remain the same (0.2 kg/m²) for all cases. The solid friction force with moving slag is much higher than for the attached cases and increases with decreasing casting speed. These predictions compare with measured data,[71] as shown in Figure 24. The agreement at lower casting speeds is consistent with the prediction that solid-slag fracture and movement increases at lower speeds. The high friction at high speed might be due to other friction sources such as excessive mold taper. Also note that for the same average solid-layer moving speed, glassy slag has higher friction than crystalline slag. It is interesting to speculate that the drop in friction at the intermediate speed might correspond to the minimum critical consumption rate and maximum safety factor predicted in this work. It implies that solid-slag-layer fracture may be more likely at both low and high casting speeds, perhaps increasing the higher average solid-layer moving speed, which would increase friction. This is consistent with measurements in Figure 24.

V. CONCLUSIONS

Analytical transient models of liquid-slag flow and solid-slag stress are developed and incorporated into a finite-difference model of heat transfer in the shell and mold (CON1D). All three models have been validated extensively with plant measurements. They are applied to study the effect of casting speed and mold-powder properties on slag-layer behavior between the oscillating mold wall and solidifying steel shell. Specific conclusions are as follows.

1. Solid slag tends to remain attached to the mold wall, especially near the meniscus. When friction on the mold side cannot compensate for the shear stress on the slag solid/liq-

(a) Slag A
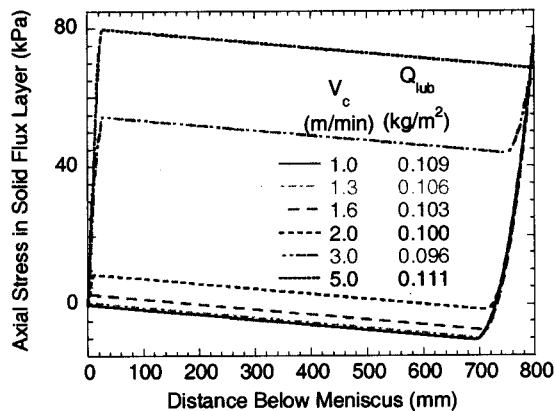
(b) Slag G

Fig. 22—(*a*) and (*b*) Effect of casting speed on solid slag fracture (no oscillation marks).

Fig. 23—Average heat flux *vs* casting speed.

Fig. 24—Effect of casting speed on friction force: measurement and prediction.

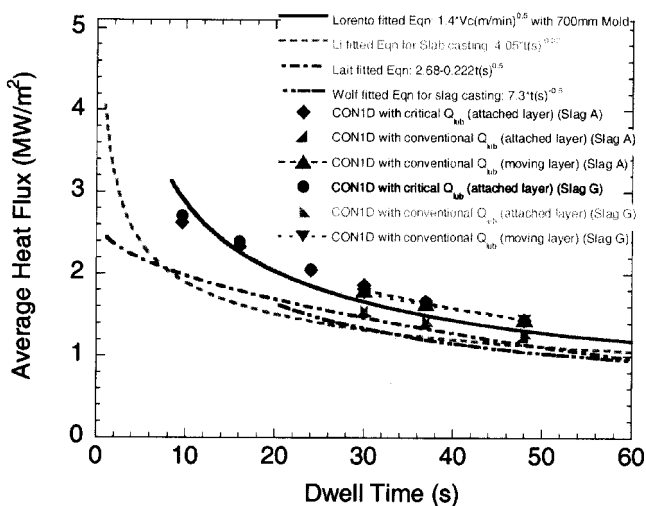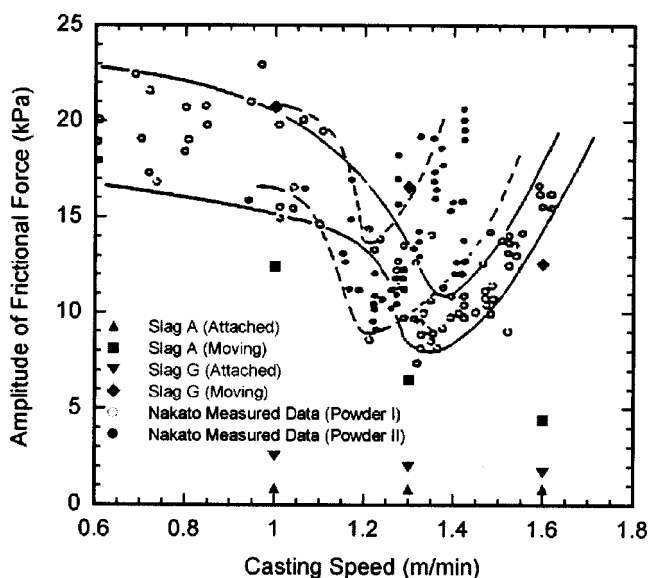uid interface, axial stress builds up in the solid slag layer. If the powder consumption rate drops below a critical level, the axial stress can exceed the slag fracture strength, so the solid slag breaks and moves down the mold wall.

2. Crystalline slag with a higher solidification temperature has a thick solid slag layer, so it lowers heat transfer across the mold/shell gap and increases the shell-surface temperature.

3. The slag temperature-viscosity curve determines the shear stress along the mold wall and affects both the critical consumption rate and possible slag fracture position. Crystalline slag (having a sharp viscosity transition) tends to fracture near the meniscus, but not easily (lower critical Q_{lub}). Glassy slag (having a gradual viscosity rise at lower temperature) tends to fracture near the mold exit and does so easily (higher critical Q_{lub}). An increasing slag solidification temperature and decreasing high-temperature viscosity (such as occurs

with high-basicity slag) tends to lower critical Q_{lub} and make it less easy to fracture.

4. The following variables lower axial stress in the solid slag layer, the critical Q_{lub} value, and the likelihood of slag fracture:

   (a) Increasing the friction coefficient helps by encouraging the solid slag to stay attached to the mold wall.

   (b) Smaller oscillation marks lower gap friction and lower the danger of slag fracture.

   (c) Decreasing the casting speed lowers critical Q_{lub} and the danger of slag fracture at the meniscus, such as for slag A and for slag G cast at high speed.

   (d) Increasing the casting speed is safer for avoiding slag fracture near the mold exit, such as for slag G cast at low speed.

   (e) Increasing the slag fracture strength helps slightly.

5. Liquid-slag-layer lubrication indicates a stable attached solid slag layer and can be recognized by a very low mold shear stress (~1 kPa) with a sinusoidal variation over each oscillation cycle.

6. The top half of the mold has negligible friction against the steel shell, as the liquid slag layer minimizes it. Solid-slag friction begins just before the liquid slag runs out, lower down the mold. Increasing the fraction of the mold with solid-slag friction can be identified by a higher total mold friction and a sharper square-wave shape of the friction curve over each cycle.

7. The high friction (10 to 20 kPa) measured in real casters might be due to any of three sources: an intermittent moving slag layer, excessive taper, or mold misalignment. At a low casting speed, the critical consumption rate is high, so variations in slag consumption at the meniscus can easily lead to solid-slag-layer fracture and movement. At a high casting speed, excessive taper and mold misalignment likely increase friction problems.

NOMENCLATURE*

d_l/d_s	liquid/solid slag-film thickness (mm)
t	time (s)
T_s	steel surface temperature (at oscillation-mark root)(°C)
T_s'	liquid slag layer hot-side temperature (°C)
V_m	mold velocity (m/s)
x	shell-thickness direction, distance from the mold wall (m)
z	casting direction, distance below the meniscus (m)
μ_s	slag viscosity at hot side of the liquid slag layer (Pa s)
σ_x	normal stress on solid slag layer (Pa)
σ_z	axial stress in solid slag layer (Pa)
τ_{max}	maximum static shear stress on mold wall (Pa)
τ_{mold}	shear stress on mold wall (Pa)
$\tau_{s/l}$	shear stress on slag solid/liquid interface (Pa)

* Other symbols are defined in Table I

REFERENCES

1. A.W.D. Hills: *J. Iron Steel Inst.,* 1965, pp. 18-26.
2. W.R. Irving: *Continuous Casting of Steel,* The Institute of Materials, London, 1993.
3. P.J. Zasowski and D.J. Sosinksy: *Steelmaking Conf. Proc.,* Detroit, MI, 25-28 Mar., 1990, ISS, Warrendale, PA, 1990, vol. 73, pp. 253-59.
4. B.G. Thomas: *1991 Steelmaking Conf.,* ISS, Warrendale, PA, 1991, pp. 69-82.
5. M.M. Wolf: in *Continuous Casting 1997,* vol. 9, *Initial Solidification and Strand Surface Quality of Peritectic Steels,* ISS/AIME, Warrendale, PA, 1997, pp. 211-22.
6. M.S. Jenkins: *Steelmaking Conf. Proc.,* Nashville, TN, 2-5 Apr., 1995, ISS/AIME, Warrendale, PA, 1995, vol. 78, pp. 669-77.
7. J.W. Cho, T. Emi, H. Shibata, and M. Suzuki: *Iron Steel Inst. Jpn. Int.,* 1998, vol. 38 (8), pp. 834-42.
8. K.C. Mills, S. Sridhar, A.S. Normanton, and S.T. Mallaband: *The Brimacombe Memorial Symp.,* Vancouver, BC, Canada, 1-4 Oct., 2000, CIMMP, Montreal, PQ, Canada, 2000, pp. 781-94.
9. T.J.H. Billany, A.S. Normanton, K.C. Mills, and P. Grieveson: *Iron-making and Steelmaking,* 1991, vol. 18 (6), pp. 403-10.
10. R. Bommaraju, R. Glennon, and M. Frazee: *1st Eur. Conf. on Continuous Casting,* Florence, Italy, 23-25 Sept., 1991, AIM, Milano, Italy, 1991, vol. 1, pp. 1.599-1.610.
11. S. Hiraki, K. Nakajima, T. Murakami, and T. Kanazawa: *77th Steel-making Conf.,* Chicago, IL, 20-23 Mar., 1994, ISS/AIME, Warrendale, PA, 1994, vol. 77, pp. 397-403.
12. J. Konishi, M. Militzer, J.K. Brimacombe, and I.V. Samarasekera: *Metall. Mater. Trans. B,* 2002, vol. 33B, pp. 413-23.
13. B.G. Thomas, A. Moitra, and R. McDavid: *Iron Steelmaker,* 1996, vol. 23 (4), pp. 57-70.
14. E. Takeuchi and J.K. Brimacombe: *Metall. Trans. B,* 1984, vol. 15B, pp. 493-509.
15. T. Araki and M. Ikeda: *Can. Metall. Q.,* 1999, vol. 38 (5), pp. 295-300.
16. C.A. Pinheiro, I.V. Samarasekera, and J.K. Brimacombe: *I&SM,* 1995, vol. 22 (2), pp. 37-39.
17. C. Orrling, S. Sridhar, Y. Kashiwaya, and A.W. Cramb: *58th Electric Furnace Conf. and 17th Process Technology Conf.,* Orlando, FL, 12-15 Nov., 2000, ISS/AIME, Warrendale, PA, 2000, pp. 211-21.
18. C.A.M. Pinheiro, I.V. Samarasekera, and B.N. Walker: *Ironmaking and Steelmaking,* 2000, vol. 27 (1), pp. 37-54.
19. B.I. Kubrik: *Steel USSR,* 1987, vol. 17 (12), pp. 573-75.
20. N.C. Machingawuta, S. Bagha, and P. Grieveson: *Steelmaking Conf. Proc.,* Washington, DC, 14-17 Apr., 1991, ISS, Warrendale, PA, 1991, vol. 74, pp. 163-70.
21. T. Cimarelli: *Metallurgia Italiana,* 1997, vol. 89 (9), pp. 31-37.
22. J. Cho, H. Shibata, T. Emi and M. Suzuki: *Iron Steel Inst. Jpn. Int.,* 1998, vol. 38 (5), pp. 440-46.
23. J.F. Chavez, A. Rodriguez, R. Morales, and V.H. Tapia: *Steelmaking Conf. Proc.,* Nashville, TN, 2-5 Apr., 1995, ISS/AIME, Warrendale, PA, 1995, vol. 78, pp. 679-86.
24. A. Yamauchi, K. Sorimachi, and T. Yamauchi: *Ironmaking and Steel-making,* 2002, vol. 29 (3), pp. 203-07.
25. D.T. Stone and B.G. Thomas: *Can. Metall. Q.,* 1999, vol. 38 (5), pp. 363-75.
26. M. Suzuki, H. Mizukami, T. Kitagawa, K. Kawakami, S. Uchida, and Y. Komatsu: *Iron Steel Inst. Jpn. Int.,* 1991, vol. 31 (3), pp. 254-61.
27. Y. Nakamori, Y. Fujikake, and K. Tokiwa: *Tetsu-to-Hagane (J. Iron Steel Inst. Jpn.),* 1984, vol. 70 (9), pp. 1262-68.
28. J.A. DiLellio and G.W. Young: *Metall. Mater. Trans. B,* 1995, vol. 26B, pp. 1225-1441.
29. M.M. Wolf: *BHM,* 2000, vol. 145 (7), pp. 270-75.
30. M.R. Ozgu and B. Kocatulum: *76th Steelmaking Conf.,* Dallas, TX, 28-31 Mar., 1993, ISS, Warrendale, PA, 1993, vol. 76, pp. 301-08.
31. G.A. Geist: *83rd Steelmaking Conf.,* Pittsburgh, PA, 26-29 Mar., 2000, ISS/AIME, Warrendale, PA, 2000, vol. 83, pp. 389-96.
32. R.J. O'Malley: *82nd Steelmaking Conf.,* Chicago, IL, 1999, vol. 82, pp. 13-33.
33. B. Mairy, D. Ramelot, and M. Dutrieux: *5th Process Technology Conf.: Measurement and Control Instrumentation in the Iron and Steel Indus-try,* Detroit, MI, 14-17 Apr., 1985, ISS/AIME, Warrendale, PA, 1985, pp. 101-17.
34. W.H. Emling and S. Dawson: *74th Steelmaking Conf.,* Washington, DG, 14-17 Apr., 1991, ISS, Warrendale, PA, 1991, vol. 74, pp. 197-217.
35. M.S. Bhamra, M.G. Charlesworth, S. Wong, D. Sawyers-Villers, and A.W. Cramb: *54th Electric Furnace Conf.,* Dallas, TX, 9-12 Dec., 1996, ISS/AIME, Warrendale, PA, 1996, vol. 54, pp. 551-64.
36. C. Orrling, A.W. Cramb, A. Tilliander, and Y. Kashiwaya: *Iron Steel-maker,* 2000, vol. 27 (1), pp. 53-63.
37. Y. Meng and B.G. Thomas: *Metall. Mater. Trans. B,* 2003, vol. 34B, pp. 685-705.
38. S. Itoyama, M. Washio, and H. Nishikawa: *Tetsu-to-Hagané (J. Iron Steel Inst. Jpn.),* 1988, vol. 74 (7), pp. 1274-81.
39. L. Hering and H.W. Fenzke: *Stahl Eisen.,* 1992, vol. 112 (7), pp. 91-95.
40. G.J.W. Kor: *Continuous Casting of Steel, 2nd Process Technology Conf.,* Chicago, IL, 23-25 Feb., 1981, ISS/AIME, Warrendale, PA, 1981, vol. 2, pp. 124-32.
41. D.R. Bland: *IMA J. Appl. Mathematics,* 1984, vol. 32, pp. 89-112.
42. H. Nakato, T. Nozaki, Y. Habu, and H. Oka: *68th Steelmaking Conf.,* Detroit, MI, 14-17 Apr., 1985, ISS/AIME, Warrendale, PA, 1985, vol. 68, pp. 361-65.
43. E. Anzai, T. Shigezumi, T. Nakano, T. Ando and M. Ikeda: *Nippon Steel Tech. Rep.,* 1987, No. 34, pp. 31-40.
44. R. Bommaraju and E. Saad: *73th Steelmaking Conf.,* Detroit, MI, 25-28 Mar., 1990, ISS, Warrendale, PA, 1990, vol. 73, pp. 281-96.
45. I.B. Risteski: *Rev. Metalurgia,* 1992, vol. 28(5), pp. 288-96.
46. J.M. Hill and Y.H. Wu: *Acta Mech.,* 1994, vol. 107 (1–4), pp. 183-98.
47. J.F. Chavez, A. Celaya, M.A. Barron, and R.D. Morales: *79th Conf. of the Steelmaking Division of the Iron and Steel Society,* Pittsburgh, PA, 24-27 Mar., 1996, ISS/AIME, Warrendale, PA, 1996, vol. 79, pp. 321-29.
48. K. Takashi, H. Sei, K. Masayuki, N. Ken, H. Kazuharu, and M. Toshihiko: *Tetsu-to-Hagané (J. Iron Steel Inst. Jpn.),* 1997, vol. 83 (11), pp. 701-06.
49. S. Ogibayashi: *85th Steelmaking Conf.,* Nashville, TN, 10-13 Mar., 2002, ISS/AIME, Warrendale, PA, 2002, vol. 85, pp. 175-83.
50. K. Nakajima: *Curr. Adv. Mater. Processing,* 1992, vol. 5 (4), pp. 1221-24.
51. P.V. Riboud, Y. Roux, L.D. Lucas, and H. Gaye: *Fachberichte Huttenpraxis Metallweiterverarbeitung,* 1981, vol. 19 (8), pp. 859-69.
52. M.D. Lanyi and C.J. Rosa: *Metall. Trans. B,* 1981, vol. 12B, pp. 287-98.
53. W.L. McCauley and D. Apelian: *Proc. 2nd Int. Symp. on Metallurgi-cal Slags and Fluxes,* AIME, Warrendale, PA, 1984, pp. 925-47.
54. K.C. Mills and S. Sridhar: *Ironmaking and Steelmaking,* 1999, vol. 26 (4), pp. 262-68.
55. *MATLAB6.1 Users Manual,* The Mathworks, Inc., Natick, MA, 2001.
56. *ANSYS6.1 Users Manual,* ANSYS, Inc., Canonsburg, PA, 2002.
57. K. Schwerdtfeger and H. Sha: *Metall. Mater. Trans. B,* 2000, vol. 31B, pp. 813-26.
58. J. Watzinger and A. Flick: *84th Steelmaking Conf.,* Baltimore, MD, 25-28 Mar., 2001, ISS/AIME, Warrendale, PA, 2001, vol. 84, pp. 205-13.
59. D. Larson: *Industrial Heating,* 1986, vol. 53 (4), pp. 16-17.
60. K.J. Lin and Y.H. Chung: *China Steel Techn. Rep.,* 1992, No. 6, pp. 71-79.
61. F. Shahbazian, D. Sichen, and S. Seetharaman: *Iron Steel Inst. Jpn. Int.,* 2002, vol. 42 (2), pp. 155-62.
62. Q. Wang, B. Xie, and J. Chi: *Conf. on Continuous Casting of Steel in Developing Countries,* Beijing, China, 14-18 Sept., 1993, CSM, Beijing, China, 1993, pp. 842-51.
63. Y. Kashiwaya, C.E. Cicutti, and A.W. Cramb: *Iron Steel Inst. Jpn. Int.,* 1998, vol. 38 (4), pp. 357-65.
64. C. Orrling, S. Sridhar, and A.W. Cramb: *Iron Steel Inst. Jpn. Int.,* 2000, vol. 40 (9), pp. 877-85.
65. M.S. Jenkins and B.G. Thomas: *Iron Steel Inst. Jpn. Int., Steelmaking Conf. Proc. 1997,* Chicago, IL, 13-16 Apr., 1997, ISS/AIME, Warrendale, PA, 1997, vol. 80, pp. 285-93.
66. S. Ogibayashi, T. Mukai, and Y. Mimura: *Nippon Steel Tech. Rep.,* 1987, No. 34, pp. 1-10.
67. K. Tsutsumi, H. Murakami, S.I. Nishioka, M. Tada, M. Nakada, and M. Komatsu: *Tetsu-to-Hagané (J. Iron Steel Inst. Jpn.),* 1998, vol. 84 (9), pp. 617-24.
68. C.A. Pinheiro, I.V. Samarasekera, and J.K. Brimacombe: *Iron Steel-maker,* 1995, vol. 22 (12), pp. 43-44.
69. H. Abratis, F. Hofer, M. Junemann, J. Sardemann, and H. Stoffel: *Stahl Eisen,* 1996, vol. 116 (9), pp. 73-78.
70. A. Yamauchi: Ph.D. Thesis, Royal Institute of Technology, Stockholm, Sweden, 2001.

71. H. Nakato, S. Omiya, Y. Habu, K. Hamagami, and T. Koshikawa: *J. Met.,* 1984, vol. 36 (3), pp. 44-50.
72. K. Hamagami, K. Sorimachi, M. Kuga, T. Koshikawa, and M. Saigusa: *Steelmaking Conf.,* 1982, vol. 65, pp. 358-64.
73. T. Okazaki, H. Tomono, K. Ozaki, and H. Akahane: *Tetsu-to-Hagané (J. Iron Steel Inst. Jpn.),* 1982, vol. 68 (10), p. 265.
74. M. Inagaki: *CAMP-ISIJ,* 1989, No. 2, p. 309.
75. B. Ho: Master's Thesis, University of Illinois, Urbana, IL, 1992.
76. D.P. Lorento: *Internal Report,* Accumold, Ontario, Canada, 2001.
77. C. Li and B.G. Thomas: *Brimacombe Memorial Symp.,* Vancouver, BC, 1-4 Oct., 2000, CIMMP, Montreal, PQ, Canada, 2000, pp. 595-611.
78. J.E. Lait, J.K. Brimacombe, and F. Weinberg: *ironmaking and Steel-making,* 1974, vol. 1 (2), pp. 90-97.
79. M.M. Wolf: *Iron Steelmaker,* 1996, vol. 23, pp. 47-51.